

# Impact of gas-based seeding on supermassive black hole populations at $z \geq 7$

Aklant K. Bhowmick<sup>1</sup>, Laura Blecha<sup>1</sup>, Paul Torrey<sup>2</sup>, Luke Zoltan Kelley<sup>3</sup>,  
Mark Vogelsberger<sup>4</sup>, Kaitlyn Kosciw<sup>1</sup>, Dylan Nelson<sup>5</sup>, Rainer Weinberger<sup>6</sup>, Lars Hernquist<sup>6</sup>

<sup>1</sup>*Dept. of Physics, University of Florida, Gainesville, FL 32611, USA*

<sup>2</sup>*Dept. of Astronomy, University of Florida, Gainesville, FL, 32611, USA*

<sup>3</sup>*Dept. of Physics and Astronomy, Northwestern University, Evanston, IL 60208, United States*

<sup>4</sup>*Dept. of Physics, Kavli Institute for Astrophysics and Space Research, Massachusetts Institute of Technology, Cambridge, MA 02139, USA*

<sup>5</sup>*Universität Heidelberg, Zentrum für Astronomie, Institut für theoretische Astrophysik, Albert-Ueberle-Str. 2, 69120 Heidelberg, Germany*

<sup>6</sup>*Harvard-Smithsonian Center for Astrophysics, 60 Garden Street, Cambridge, MA 02138, USA*

16 February 2022

## ABSTRACT

Deciphering the formation of supermassive black holes (SMBHs) is a key science goal for upcoming observational facilities. In many theoretical channels proposed so far, the seed formation depends crucially on local gas conditions. We systematically characterize the impact of a range of gas-based black hole seeding prescriptions on SMBH populations using cosmological simulations. Seeds of mass  $M_{\text{seed}} \sim 10^3 - 10^6 M_{\odot}/h$  are placed in halos that exceed critical thresholds for star-forming, metal-poor gas mass and halo mass (defined as  $\tilde{M}_{\text{sf,mp}}$  and  $\tilde{M}_{\text{h}}$ , respectively, in units of  $M_{\text{seed}}$ ). We quantify the impact of these parameters on the properties of  $z \geq 7$  SMBHs. Lower seed masses produce higher black hole merger rates (by factors of  $\sim 10$  and  $\sim 1000$  at  $z \sim 7$  and  $z \sim 15$ , respectively). For fixed seed mass, we find that  $\tilde{M}_{\text{h}}$  has the strongest impact on the black hole population at high redshift ( $z \gtrsim 15$ , where a factor of 10 increase in  $\tilde{M}_{\text{h}}$  suppresses merger rates by  $\gtrsim 100$ ). At lower redshift ( $z \lesssim 15$ ), we find that  $\tilde{M}_{\text{sf,mp}}$  has a larger impact on the black hole population. Increasing  $\tilde{M}_{\text{sf,mp}}$  from 5 – 150 suppresses the merger rates by factors of  $\sim 8$  at  $z \sim 7 - 15$ . This suggests that the seeding criteria explored here could leave distinct imprints on LISA merger rates. In contrast, AGN luminosity functions are much less sensitive to seeding criteria, varying by factors  $\lesssim 2 - 3$  within our models. Such variations will be challenging to probe even with future sensitive instruments such as Lynx or JWST. Our study provides a useful benchmark for development of seed models for large-volume cosmological simulations.

**Key words:** (galaxies:) quasars: supermassive black holes

## 1 INTRODUCTION

Supermassive black holes (SMBHs) are now believed to reside in almost every massive galaxy in the Universe (Kormendy & Richstone 1992; Harms et al. 1994; Miyoshi et al. 1995). The scaling relations between the mass of the local SMBH and their host galaxy properties (e.g., stellar mass or velocity dispersion; Magorrian et al. 1998; Ferrarese & Merritt 2000; Gebhardt et al. 2000; Kormendy & Ho 2013; Davis et al. 2017) suggest that their evolution is closely connected to the evolution of the host galaxies; these relations have been found to persist up to  $z \sim 1.5$  (Ding et al. 2020). Determining the redshifts at which these scaling relations were first established is an open problem, and is crucial to understanding SMBH formation and their subsequent evolution in relation to their host galaxies. That being said, recent simulations do suggest that these scaling relations may persist at redshifts as high as  $z \sim 10$  (Huang et al. 2018), which is not very long after the epoch of seed formation. This hints that “seeds” of SMBHs may influence the assembly of the earliest

galaxies in our Universe. However, little is known about the formation mechanisms of these black hole seeds; this a major outstanding problem in astrophysics.

This is accordingly one of the key science goals of the next generation observational facilities targeting the high redshift ( $z \sim 6 - 15$ ) universe, including the James Webb Space Telescope (JWST; Gardner et al. 2006), the Nancy Graham Roman Space telescope (NGRST, formerly WFIRST; Spergel et al. 2015), the Lynx X-ray Observatory (The Lynx Team 2018), and the Laser Interferometer Space Antenna (LISA; Baker et al. 2019). Additionally, signatures of low to intermediate mass BHs ( $\lesssim 10^6 M_{\odot}/h$ ) are being identified in an increasing number of  $z \sim 0$  dwarf galaxies, see Reines et al. 2013; Marleau et al. 2017; Schutte et al. 2019); this hints at the possibility that imprints of seed formation may also be present in these galaxies.

Various channels of seed formation have been proposed so far. Remnants of Population III (Pop III) stars (Fryer et al. 2001; Madau & Rees 2001; Xu et al. 2013; Smith et al. 2018)

may form “light” seeds with masses of  $\sim 100 M_{\odot}$ . Intermediate mass seeds ( $\sim 10^2 - 10^3 M_{\odot}$ ) could be formed via runaway collisions of stars in dense nuclear star clusters or NSCs (Davies et al. 2011; Lupi et al. 2014; Kroupa et al. 2020; Das et al. 2021b,a). Massive seeds ( $\sim 10^5 - 10^6 M_{\odot}$ ) could be formed in atomic cooling haloes via direct collapse (DCBHs) of pristine, low angular momentum gas in the presence of Lyman Werner (LW) UV radiation that can prevent  $H_2$  cooling (Bromm & Loeb 2003; Begelman et al. 2006; Regan et al. 2014; Latif et al. 2016; Luo et al. 2018; Wise et al. 2019; Luo et al. 2020). Lastly, primordial black hole seeds ( $10^2 - 10^5 M_{\odot}/h$ ) from the early universe may also contribute to SMBH populations (Rubin et al. 2001; Khlopov et al. 2002, 2005; Kawasaki et al. 2012; Bernal et al. 2018; Belotsky et al. 2019).

The discovery of a population of high redshift ( $z \gtrsim 6$ ) quasars (with masses of  $10^8 - 10^9 M_{\odot}$ ; Fan et al. 2001; Mortlock et al. 2011; Wu et al. 2015; Bañados et al. 2018) poses a significant challenge to all these scenarios. This challenge has only become more severe with recent discoveries of massive quasars at  $z \geq 7$ , including the current record-holder at  $z = 7.642$ , a mere  $\sim 700$  Myr after the Big Bang (Wang et al. 2021). For example, low mass ( $\sim 10^2 M_{\odot}$ ) Pop III seeds require sustained Eddington or super-Eddington accretion to grow by seven orders of magnitude and form a  $\sim 10^9 M_{\odot}/h$  quasar by  $z \sim 6 - 7$ . This is difficult to achieve even under optimal growth conditions such as a steady supply of gas and inefficient radiative feedback (e.g., Pacucci et al. 2015). On the other hand, DCBH seeds may have a better chance of growing into the first quasars as they may form with higher initial masses in regions with significantly higher gas densities. However, the conditions required for their formation are difficult to meet because of the necessary presence of UV radiation from nearby star-forming galaxies, which can contaminate the region with metals before any direct collapse can occur. In a nutshell, all of these proposed seed models present challenges for producing the observed population of SMBHs. This leaves us with a large, unconstrained parameter space of possible seed models that need to be assessed for their ability to explain the observed SMBH population (including the first quasars).

In order to use the future observational facilities to constrain black hole seed models, it is crucial to identify their imprints on the observable properties of SMBHs and their host galaxies. For example, LISA will be able to measure merger rates at redshifts  $z \gtrsim 10$  for black hole masses a little below  $\sim 10^4 M_{\odot}/h$  (Amaro-Seoane et al. 2017); we therefore need to characterize the theoretical predictions for these merger rates from different models in order to properly interpret the LISA measurements. To that end, many studies have been performed to date using semi-analytic models (SAMs; e.g., Sesana et al. 2007; Volonteri & Natarajan 2009; Barausse 2012; Valiante et al. 2018; Ricarte & Natarajan 2018; Dayal et al. 2019; DeGraf & Sijacki 2020). SAMs are efficient in terms of speed and memory usage, enabling such studies to systematically explore a wide range of seed model parameters. Overall, SAMs predict strong signatures of black hole seed models at high redshifts ( $z \gtrsim 7$ ), particularly for low mass BH merger rates and, to a lesser extent, the faint end of the luminosity function of active galactic nuclei (AGN). As an example, Ricarte & Natarajan (2018) showed that light seeds produce a significantly higher number of low luminos-

ity ( $\lesssim 10^{42}$  ergs/s) AGN and low mass ( $\lesssim 10^4 M_{\odot}$ ) black hole mergers compared to heavy seeds at  $z \gtrsim 6$ . That being said, an inevitable limitation of SAMs is that they are unable to accurately capture the internal structure and dynamics of galaxies. The detailed local environment determines the gas inflows that supply fuel for black hole seed formation and accretion, and it can therefore have a significant impact on the black hole masses and luminosities. These effects can only be captured in a hydrodynamical simulation.

Cosmological hydrodynamical simulations have emerged as powerful tools to study galaxy formation and SMBH growth (Di Matteo et al. 2012; Sijacki et al. 2015; Khandai et al. 2015; Schaye et al. 2015; Volonteri et al. 2016; Dubois et al. 2016; Kaviraj et al. 2017; Tremmel et al. 2017; Nelson et al. 2019a; Volonteri et al. 2020). They provide us with the unique ability to understand how the different components of our contemporary galaxy formation models (star formation, enrichment, feedback, SMBH growth) interact with the complex gas dynamics (see also Vogelsberger et al. 2020 for recent review of the current status of cosmological simulations). The fact that black hole growth is profoundly impacted by the surrounding gas (and vice versa) makes simulations an indispensable tool for exploring the impact of black hole seed models. Because they have a substantially higher computational demand compared to SAMs, modeling black hole seed formation in cosmological hydrodynamic simulations presents a unique set of challenges. A key limitation is the mass and spatial resolution. For most state-of-the-art large-volume cosmological simulations, densest gas cells in a halo are typically converted to black hole seeds based on a prescribed set of seeding conditions; this naturally implies that the minimum value for the seed mass is limited by the gas mass resolution which is typically  $\sim 10^5 - 10^6 M_{\odot}/h$ . At the same time, a lower mass resolution of dark matter and star particles (relative to the black hole seed mass) can also lead to dynamical instabilities (Tremmel et al. 2015); this is typically dealt with by repositioning the black holes to the local potential minima in their immediate vicinity. Smaller-volume simulations including zoom-in simulations of individual halos can achieve substantially higher resolution, but this comes at the expense of statistical power and cosmic variance, especially for rare objects such as DCBHs.

Moreover, even high-resolution simulations must still rely on sub-grid models for unresolved physical processes such as star formation and chemical enrichment. Due to all these complexities, most current cosmological simulations do not model black hole seeds based on gas properties. Instead, they seed BHs (of mass  $\sim 10^5 - 10^6 M_{\odot}/h$ ) based on a threshold halo mass (typically  $\sim 10^{10} M_{\odot}/h$ ). These simple halo mass based prescriptions have been largely successful in reproducing properties of local SMBHs (Khandai et al. 2015; Mutlu-Pakdil et al. 2018; Weinberger et al. 2018). Additionally, the largest volume (400 Mpc/h comoving box length) cosmological hydrodynamic simulations such as BlueTides (Feng et al. 2016) have also been able to reproduce the  $z \gtrsim 7$  quasars using a similar halo based seed model (Ni et al. 2018; Teneti et al. 2019; Marshall et al. 2020). However, these models are not able to distinguish between different seed formation channels. Therefore, the next natural step is to develop realistic gas-based black hole seeding prescriptions (representing the different seed formation channels) for the next generation of cosmological simulations.

Efforts to incorporate gas-based seeding prescriptions have begun in the last few years. For example, the **ROMULUS** simulation (Tremmel et al. 2017) produces  $10^6 M_\odot/h$  seed black holes from gas cells that have low metal fractions ( $Z \lesssim 10^{-4} Z_\odot$ ), density higher than 15 times the star formation threshold, and temperatures of  $\sim 10^4$  K. The **Horizon-AGN** simulation (Volonteri et al. 2016; Kaviraj et al. 2017) seeds  $10^5 M_\odot/h$  black holes in regions with gas and stellar densities higher than a chosen threshold, and stellar velocity dispersion  $> 100$  km/s. While there are several such recent works implementing physically motivated seeding prescriptions (other examples include Bellovary et al. 2011; Dubois et al. 2013; Hirschmann et al. 2014; Taylor & Kobayashi 2015; Habouzit et al. 2017; Davé et al. 2019; Lee et al. 2020; Trebitsch et al. 2020), the vast parameter space of models consistent with PopIII, NSC and DCBH channels have yet to be systematically explored at a similar level as that of SAMs. To that end, the recent study of Zhu et al. (2020) does systematically explore seed masses from 10 to  $10^6 M_\odot$ . However, their work is a somewhat broader exploration of a variety of black hole models (including accretion and feedback) to reproduce the most luminous  $z > 6$  quasars, instead of explicitly focusing on gas-based seeding and its impact on the wider SMBH population. Additionally, they had to use sub-resolution recipes for the treatment of seed masses smaller than their gas mass resolution ( $6.5 \times 10^5 M_\odot/h$ ). Given all these developments, the time is ripe for a systematic exploration of gas-based seed models at resolutions high enough to fully resolve black hole seeds. In this study, we utilize zoom-in cosmological hydrodynamic simulations to resolve seed masses down to  $\sim 10^3 M_\odot$ .

This paper is first in a series of works dedicated towards conducting a systematic parameter study of the impact of gas-based seeding prescriptions on the high redshift ( $z \gtrsim 7$ ) black hole population. We explore the parameter space of seed models using zoom simulations. black holes are seeded in sufficiently massive halos with pristine star forming gas, which is a common feature amongst Pop III, NSC and DCBH channels. We also emphasize that our numerical seed models are completely agnostic about which seed parameters correspond to which physical channel. Different parts of the parameter space may be more (or less) representative of different physical channels. Our approach has a unique advantage of being able to traverse the parameter space to explore many of the possible channels in the process (note that primordial black hole seeds are not within the scope of our models). We quantify the impact of the various seed parameters on the key black hole observables such as the stellar mass vs. black hole mass ( $M_* - M_{bh}$ ) relation, black hole mass functions, luminosity functions and merger rates.

The structure of the paper is as follows: Section 2 describes our basic methodology, and Section 3 describes our simulation suite. Section 4 compares our predictions with existing observational constraints. Section 5 focuses on the impact of our seed models on  $z \gtrsim 7$  SMBH populations. Section 6 investigates the resolution convergence. Finally, we summarize our key findings in Section 7.

## 2 METHODS

Our simulations were run using the **AREPO** (Springel 2010; Pakmor et al. 2011, 2016; Weinberger et al. 2020) moving-

mesh magneto-hydrodynamics (MHD) code. The code solves for gravity coupled with MHD. The gravity solver uses the PM-tree method (Barnes & Hut 1986) and the MHD solver uses a non-static unstructured grid formed by performing a Voronoi tessellation of the domain. **AREPO** has been used to produce simulations of the Universe at a wide range of scales. At the largest scales, we have uniform volume cosmological simulations such as the Illustris (Vogelsberger et al. 2014a; Genel et al. 2014; Nelson et al. 2015; Sijacki et al. 2015) and IllustrisTNG (Pillepich et al. 2018b; Nelson et al. 2018; Marinacci et al. 2018; Naiman et al. 2018; Springel et al. 2018; Pillepich et al. 2019; Nelson et al. 2019a,b) suites. These simulations have box sizes ranging from  $\sim 50$  Mpc to  $\sim 300$  Mpc and baryonic mass resolutions ranging from  $\sim 10^5 - 10^7 M_\odot$ . They have been largely successful in producing galaxy and SMBH populations consistent with observations, in Illustris (Vogelsberger et al. 2014b; Sales et al. 2015; Sijacki et al. 2015) and in TNG (Weinberger et al. 2018; Pillepich et al. 2018b; Genel et al. 2018; Donnari et al. 2019; Torrey et al. 2019; Rodriguez-Gomez et al. 2019; Übler et al. 2021; Habouzit et al. 2021). At the smallest scales, we have cosmological zoom simulation suites such as AU-RIGA (Grand et al. 2017) for individual milky-type galaxies, and HESTIA (High-resolutions Environmental Simulations of The Immediate Area) (Libeskind et al. 2020) for the Local Group. These simulations have been successful in reproducing observational results for the internal structures of galaxies (Cautun et al. 2020; Blázquez-Calero et al. 2020; Grand et al. 2020). All these developments make **AREPO** an ideal tool for the development of black hole models, which require a reliable modeling of the necessary physics over a large dynamic range.

In addition to gravity and MHD, **AREPO** is equipped with a wide range of “sub-resolution” physics models. In this work, we adopt the fiducial IllustrisTNG galaxy formation model (Weinberger et al. 2017; Pillepich et al. 2018a) as our baseline model, with the obvious exception of modified black hole seed models (described in the next section). Here we summarize some of the key features of our modeling that do not deviate from the IllustrisTNG model:

- Multiphase star forming gas is modeled using an sub-grid pressurization prescription (Springel & Hernquist 2003). When the densities of the gas cells exceed a threshold of  $0.13 \text{ cm}^{-3}$ , star particles are stochastically formed with an associated free-fall time scale of 2.2 Gyr.
- Stellar evolution is implemented as described in Vogelsberger et al. (2013), with updates for TNG as described in Pillepich et al. (2018a). Briefly, each star particle is assumed to represent a single stellar population (SSP) with a fixed formation time and metallicity, with an initial mass function (IMF) adopted from Chabrier (2003). Stars return mass and metals to the nearby ISM gas following SNIa, SNII, and AGB stars. The abundances of nine species (H, He, C, N, O, Ne, Mg, Si, Fe) are individually tracked.
- Metal cooling is included in the presence of a spatially uniform and ionizing UV background, along with self-shielding in dense gas (Vogelsberger et al. 2013).
- Stellar feedback and supernovae Type II in particular produce galactic-scale winds (Pillepich et al. 2018a).
- Magnetic fields are included by initializing with a small ( $\sim 10^{-14}$  comoving Gauss) seed magnetic field at an

arbitrary orientation. Further evolution of the magnetic field is determined by the MHD equations (Pakmor et al. 2011).

- Black hole accretion is modeled using the Eddington limited Bondi-Hoyle formula given by

$$\dot{M}_{\text{BH}} = \min(\dot{M}_{\text{Bondi}}, \dot{M}_{\text{Edd}}) \quad (1)$$

$$\dot{M}_{\text{Bondi}} = \frac{4\pi G^2 M_{\text{BH}}^2 \rho}{c_s^3} \quad (2)$$

$$\dot{M}_{\text{Edd}} = \frac{4\pi G M_{\text{BH}} m_p}{\epsilon_r \sigma_T} c \quad (3)$$

where  $G$  is the gravitational constant,  $M_{\text{BH}}$  is the mass of the BH,  $\rho$  is the local gas density,  $c_s$  is the local sound speed of the gas,  $m_p$  is the mass of the proton,  $\epsilon_r$  is the radiative efficiency and  $\sigma_T$  is the Thompson scattering cross section. Accreting black holes have a bolometric luminosity given by

$$L = \epsilon_r \dot{M}_{\text{BH}} c^2, \quad (4)$$

where  $\epsilon_r = 0.2$  is the radiative efficiency.

- AGN feedback is implemented in two modes. If the Eddington ratio  $\eta \equiv \dot{M}_{\text{bh}}/\dot{M}_{\text{edd}}$  is higher than a critical value of  $\eta_{\text{crit}} = \min[0.002(M_{\text{BH}}/10^8 M_{\odot})^2, 0.1]$ , the feedback is deposited in the form of thermal energy that is acquired by the neighboring gas at a rate given by  $\epsilon_{f,\text{high}} \epsilon_r \dot{M}_{\text{BH}} c^2$  where  $\epsilon_{f,\text{high}} \epsilon_r = 0.02$ .  $\epsilon_{f,\text{high}}$  is called the “high accretion state” coupling efficiency. If the Eddington ratio is lower than the critical value, the feedback is deposited in the form of kinetic energy that is injected into the gas at irregular time intervals. The kinetic energy manifests as a ‘wind’ oriented along a randomly chosen direction. The injected energy is given by  $\epsilon_{f,\text{low}} \dot{M}_{\text{BH}} c^2$  where  $\epsilon_{f,\text{low}}$  is called the ‘low accretion state’ coupling efficiency.  $\epsilon_{f,\text{low}}$  has a maximum value of 0.2, with smaller values at very low gas densities. For further details on the AGN feedback implementation, interested readers are encouraged to refer to Weinberger et al. (2017).

- The small-scale dynamics of black holes cannot be resolved accurately, particularly when the black hole mass is close to the gas mass resolution of the simulation. Due to this, at each time step, the black holes are “re-positioned” on to the potential minimum within a sphere enclosing  $10^3$  neighboring gas cells (same as IllustrisTNG).

- Two black holes are promptly merged when their separations are within a distance  $R_{bh}$  of at least one of the BHs; here, the  $R_{bh}$  is defined to be the minimum radius of a sphere that encloses a specified number (weighted over a smoothing kernel) of neighboring gas cells; these are listed in Table 1 for different simulation resolutions and correspond to typical  $R_{bh}$  values of  $\sim 8$  kpc/h. Note that this “neighbor search radius” also governs the accretion and feedback properties of the BH. In particular, the density averaged over the neighboring gas cells determines the accretion rate as specified by Eq. (3). Furthermore, energy from black hole feedback is also injected into the same set of neighboring gas cells.

## 2.1 Gas-based modeling of black hole seeds

Here, we describe how the black holes are seeded in our simulations based on the gas properties inside halos. Most seed formation channels that have been proposed so far have three features in common; they occur in regions with high gas density (at or above the threshold for star formation), low metallicity, and deep gravitational potentials (Volonteri 2012; Sesana 2012).

Motivated by these considerations, we assume a 3-parameter family of seed models. More specifically, a black hole of seed mass  $M_{\text{seed}}$  is inserted in a halo if the following two conditions are met:

- The total mass of star forming, metal poor gas in the halo exceeds a critical threshold denoted by  $\tilde{M}_{\text{sf,mp}}$ . Subscripts ‘sf’ and ‘mp’ denote ‘star forming’ and ‘metal poor’ respectively. The tilde ( $\sim$  symbol) denotes that this quantity is in the units of  $M_{\text{seed}}$ .

- The total mass of the halo exceeds a critical threshold denoted by  $\tilde{M}_{\text{h}}$ . Here again, the tilde ( $\sim$  symbol) denotes that it is in the units of  $M_{\text{seed}}$ .

If the above two conditions are met, the densest gas cell (hereafter referred to as “parent gas cell”) in the halo is converted to a seed BH. “Metal poor” gas cells are defined as those having metallicities less than  $10^{-4} Z_{\odot}$  (note that the primordial metallicity is assumed to be  $6.29 \times 10^{-8} Z_{\odot}$  as in IllustrisTNG). This value is chosen because: 1) it is within the regime of Pop III stars ( $\lesssim 10^{-3} Z_{\odot}$ ), and 2) metal line cooling can be sufficiently suppressed at these metallicities for a direct collapse to occur (Chon & Omukai 2020). With this choice, our gas-based seed models are broadly consistent with physical conditions typical of all possible seed formation channels (PopIII, NSC and DCBH). That being said, we also note that our results are not sensitive to this metallicity threshold for values ranging between  $10^{-5} - 10^{-2} Z_{\odot}$ . This is because the stellar and gas metallicities in our simulation rapidly exceeds  $\sim 10^{-3} Z_{\odot}$  due to the limited time resolution of our simulation compared to the stellar evolution time scales post main sequence.

Overall, our final model contains three key variable parameters, namely  $M_{\text{seed}}$ ,  $\tilde{M}_{\text{sf,mp}}$ , and  $\tilde{M}_{\text{h}}$ . Our paper is primarily focused on systematically exploring the influence of these seed parameters on the resulting SMBH populations. Of course, these three parameters alone do not fully represent all possible physically motivated seeding channels; rather, this work is meant to provide a systematic analysis of how the basic halo and gas properties impact the SMBH population, which will inform future models that may include additional physics (e.g. seeding based on LW intensities and infall rates of gas towards halo centers).

### 2.1.1 Additional seeding criteria: Preventing spurious seeds and mergers

As noted earlier, black holes in our simulations are repositioned on the potential minimum of their host halos to prevent dynamical artifacts from numerical noise. Along the same lines, black hole pairs are promptly merged when their separation falls below the spatial resolution scale. To avoid potential unphysical situations caused by this, we have imposed a few additional seeding conditions:

- First, there are scenarios where a halo may want to seed a new BH, but that BH’s neighbor search radius ( $R_{bh}$ ) would immediately include another black hole. Thus, if a new black hole were seeded, it would immediately merge. This problem is exacerbated for smaller black hole seeds; this is because they form in lower mass halos which are more abundant and generally smaller in size, increasing the likelihood for the neighbor search radii to overlap with nearby halos.



Additionally, the neighbor search radii (for fixed number of neighbors) in lower mass halos are also typically larger than in higher mass halos due to lower gas densities. We therefore prevent this by not allowing the formation of any new seeds if their parent gas cells are within the neighbor search radius of pre-existing black holes.

(ii) Second, there can also be scenarios where a halo can artificially lose a BH (via re-positioning and prompt merger) during a close encounter with a much larger halo (and much deeper potential). If the encounter turns out to be a “fly-by” (and does not lead to a halo merger), then the halo will get re-seeded with a new BH. This overall leads to an artificial increase in the number of black hole seeds and black hole mergers. While we cannot prevent the halo from losing its black hole with the current black hole re-positioning scheme, we can certainly prevent the creation of new “spurious” seeds. In order to do that, we “tag” the neighboring gas cells of every newly seeded halo; this retains the memory of past seeding events in halos. We then compute the amount of “tagged gas” in a halo at a given time step, and use it as a proxy to determine if the halo contains imprints of a past seeding event. We thereby prevent re-seeding from occurring in those halos. Appendix A contains the full details of this implementation and demonstrates that if we do not suppress these spurious seeds, the merger rates can be overestimated by up to factors of  $\sim 10$ .

### 3 SIMULATION OVERVIEW

#### 3.1 Zoom simulation suite

We apply the black hole seeding methods described in the previous subsection to a suite of cosmological zoom-in simulations targeted at helping us understanding the impact of gas-based black hole seeding. Therefore, our simulation suite mainly consists of these zoom runs with a parent volume of  $(25 \text{ Mpc}/h)^3$ . The cosmology is based on the results of Planck Collaboration et al. (2016), i.e.  $\Omega_\Lambda = 0.6911$ ,  $\Omega_m = 0.3089$ ,  $\Omega_b = 0.0486$ ,  $H_0 = 67.74 \text{ km sec}^{-1}\text{Mpc}^{-1}$ ,  $\sigma_8 = 0.8159$ ,  $n_s = 0.9667$ . The simulations were initialized at  $z = 127$  using the MUSIC (Hahn & Abel 2011) initial condition generator.

The resolution of the background grid and high-resolution zoom regions are characterized by parameters we refer to as  $L_{\min}$  (levelmin) and  $L_{\max}$  (levelmax), respectively. The resolution level,  $L$ , is defined such that a uniform-resolution box with the same mass resolution would have  $2^L$  DM particles per side. We set  $L_{\min} = 7$  for the background grid, which corresponds to a DM mass resolution of  $5.3 \times 10^9 M_\odot/h$ . For the high resolution zoom region, we consider  $L_{\max}$  values ranging from 9 to 12. Additionally, we also have a buffer region comprising of DM particles at intermediate resolutions between the background grid and the zoom region; this buffer region enables a smooth transition between zoom region to background grid. The details of the mass and spatial resolution for various values of  $L_{\max}$  are shown in Table 1. For the highest resolution runs with  $L_{\max} = 12$ , the DM mass resolution is  $1.6 \times 10^4 M_\odot/h$  and gas mass resolution is  $\sim 10^3 M_\odot/h$  (note that masses of gas cells depend on the extent of refinement or derefinement of the Voronoi cells). However, the  $L_{\max} = 12$  simulations have significant computational expense, and we

only run a select few of them in order to 1) resolve seed masses of  $\sim 10^3 M_\odot$  and to 2) investigate resolution convergence. We demonstrate in Section 6 that our simulations approach resolution convergence for  $L_{\max} \geq 11$ . Therefore, the majority of our seed parameter space is explored using  $L_{\max} = 11$  simulations, which have a gas mass resolution of  $\sim 10^4 M_\odot/h$ .

##### 3.1.1 The parameter space ( $M_{\text{seed}}$ , $\tilde{M}_{\text{sf,mp}}$ , $\tilde{M}_h$ ) of seed models

The seed masses  $M_{\text{seed}}$  range from  $8 \times 10^5$  to  $1.56 \times 10^3 M_\odot/h$ , as listed in Table 1. Note that the minimum seed mass that can be probed at each  $L_{\max}$  is limited by the gas mass resolution of the simulation. For example, at  $L_{\max} = 10$ , we can explore only seed masses  $\geq 1 \times 10^5 M_\odot/h$ . But at the highest resolution of  $L_{\max} = 12$ , we can explore seed masses  $\geq 1.56 \times 10^3 M_\odot/h$ . The differences in mass resolution between successive values of  $L_{\max}$  is roughly a factor of 8; for this reason we also vary  $M_{\text{seed}}$  by multiples of 8.

The parameter  $\tilde{M}_{\text{sf,mp}}$  is a multiplicative factor that (when multiplied by  $M_{\text{seed}}$ ) determines how much of the star forming, metal poor gas mass is required to form a black hole seed of mass  $M_{\text{seed}}$ . A larger value of  $\tilde{M}_{\text{sf,mp}}$  therefore corresponds to a lower efficiency for converting pristine star-forming gas into black hole seeds. This efficiency may depend on the seed formation channel as well as the halo properties (e.g., mass, concentration, or spin), but there are currently no empirical constraints. We choose to explore values of  $\tilde{M}_{\text{sf,mp}} = 5, 50, 150$  which correspond to seed formation efficiencies of 20, 2, 0.7%, respectively.

The parameter  $\tilde{M}_h$  is similarly a multiplicative factor that, when multiplied by  $M_{\text{seed}}$ , sets the minimum threshold halo mass for the formation of black hole seeds. We explore values of  $\tilde{M}_h = 10^3$ ,  $3 \times 10^3$  &  $10^4$ . Previous work (Yoshida et al. 2003; Kulkarni et al. 2020) has shown that the critical halo mass for the collapse of molecular gas clouds is  $\sim 10^5 - 10^6 M_\odot$ . If Pop III seeds of  $10^2 M_\odot$  form in halos above these critical masses, this corresponds to  $\tilde{M}_h \sim 10^3 - 10^4$ . At the other end, direct collapse of gas can allow formation of  $\sim 10^4 - 10^5 M_\odot$  black holes in atomic cooling halos of masses close to  $\sim 10^7 - 10^8 M_\odot$ , again corresponding to  $\tilde{M}_h \sim 10^3 - 10^4$  (this is broadly based on results of Wise et al. 2019 and Regan et al. 2020). Therefore, our choice of varying  $\tilde{M}_h$  from  $10^3 - 10^4$  is reasonable for an initial exploration of the parameter space. That being said, we do not rule out models with  $\tilde{M}_h$  higher than  $10^4$ , but they would form too few black holes within our zoom volume to robustly predict the statistical properties of SMBH populations.

##### 3.1.2 Target regions for high resolution zoom-ins

Our suite is comprised of two target regions. We first run a low resolution uniform volume simulation with 25 Mpc/h box-size and  $128^3$  particles ( $L_{\min} = L_{\max} = 7$ ) from  $z = 127$  to  $z = 0$ . Our parent box-size is large enough to produce target regions that are sufficiently overdense to allow formation of a significant number of seeds. Larger box-sizes would allow us to simulate more extreme regions, but at significantly higher computational expense. We select two target regions from our uniform box as follows:

$L_{\max}$	$M_{dm} (M_{\odot}/h)$	$M_{gas} (M_{\odot}/h)$	$\epsilon (kpc/h)$	Black hole neighbors	Allowed $M_{seed} (M_{\odot}/h)$ values
9	$8.4 \times 10^6$	$\sim 10^6$	1	32	$8 \times 10^5$
10	$1 \times 10^6$	$\sim 10^5$	0.5	64	$8 \times 10^5, 1 \times 10^5$
11	$1.3 \times 10^5$	$\sim 10^4$	0.25	128	$8 \times 10^5, 1 \times 10^5, 1.25 \times 10^4$
12	$1.6 \times 10^4$	$\sim 10^3$	0.125	256	$8 \times 10^5, 1 \times 10^5, 1.25 \times 10^4, 1.56 \times 10^3$

**Table 1.** Spatial and mass resolutions within the zoom region of our simulations for various values of  $L_{\max}$  (see Section 3 for the definition).  $M_{dm}$  is the mass of a dark matter particle,  $M_{gas}$  is the typical mass of a gas cell (note that gas cells can refine and de-refine depending on the local density), and  $\epsilon$  is the gravitational smoothing length. The 4th column represents the number of nearest gas cells that are assigned to be black hole neighbors. The 5th column corresponds to the seed masses allowed at each  $L_{\max}$ , which is limited by the gas mass resolution.

• Our primary target region is focused on making predictions for the high redshift universe ( $z \gtrsim 7$ ). We select a target halo of mass  $3.5 \times 10^{11} M_{\odot}/h$  at  $z = 5$  (corresponding to a peak height<sup>1</sup> of  $\nu = 3.3$ ) and trace its DM particles to  $z = 127$ . We then construct a cubical volume with minimum dimensions required to enclose the particles, and assign it to be the initial zoom volume at  $z = 127$  (one could alternatively choose an ellipsoid or convex hull, but this would not impact our main results). We shall hereafter refer to this region as **ZOOM\_REGION\_z5**. Figures 1 and 2 show the density and metallicity profiles for **ZOOM\_REGION\_z5** at various redshift snapshots between  $z = 20$  to  $z = 8$ . As the density increases, star formation ensues and that is soon followed by formation of seed black holes. The subsequent stellar evolution processes lead to the onset of metal enrichment; the metals continue to disperse throughout the region and eventually suppresses the formation of new black holes at  $z \sim 11 - 12$  (this is demonstrated more quantitatively in Section 6). The number of seeds that form in this region (up to  $z \sim 7$ ) range from  $\sim 5 - 1000$  depending on the seed mass; models with lower  $M_{seed}$ ,  $\tilde{M}_h$  &  $\tilde{M}_{sf,mp}$  naturally lead to a higher number of seeds (we shall quantify these trends in Section 5.1).

• Our secondary target region is focused on making predictions at  $z = 0$  and comparing against observational constraints. We follow the same procedure as **ZOOM\_REGION\_z5**, but for a target halo of mass  $6.4 \times 10^{11} M_{\odot}/h$  at  $z = 0$  (this corresponds to a peak height of  $\nu = 0.8$ ). We choose a lower density region (compared to **ZOOM\_REGION\_z5**) to reduce the computational expense of running simulations to  $z = 0$ . We shall hereafter refer to this region as **ZOOM\_REGION\_z0**. The number of seeds formed in **ZOOM\_REGION\_z0** is  $\sim 50\%$  fewer than that of **ZOOM\_REGION\_z5**.

The peripheral regions of the zoom volume are inevitably susceptible to contamination from low resolution DM particles. Note that our halo mass criterion for seeding is based on the mass contributed exclusively by the highest resolution DM particles; as a result, most ( $\gtrsim 95\%$ ) of our black holes seed in regions which have negligible levels ( $\lesssim 1\%$ ) of contamination from low resolution DM particles. However, as the region undergoes gravitational collapse, some black

holes inevitably end up in halos which are contaminated by low resolution particles. When the host halos (BH environments) are contaminated, the accretion rates (and therefore also their masses and luminosities) are susceptible to numerical artifacts. We find that within  $1 \text{ Mpc}/h$  from the center of mass (COM) of the zoom volume, there is virtually no contamination at all redshifts above  $z \gtrsim 7$ . Therefore, when analyzing the final black hole masses and luminosities at various snapshots in Sections 5.3 and 5.5, we include only those BHs (at each snapshot) which are within  $1 \text{ Mpc}/h$  from the center of mass of the zoom volume. By doing this, we exclude  $\sim 70\%$  of all black holes at  $z \sim 7$  (the percentage decreases at higher redshifts); while this is a significant amount, the remaining black holes are assured to have masses and luminosities that are not impacted by numerical artifacts. Note however that for analysing the number of seeding and merger rates in Sections 5.1 and 5.4 respectively, we include all the events that occur within our zoom volume. The seeding frequency is not significantly impacted by low resolution contamination because most seeds do start out in regions with negligible contamination. As for the merger rates, due to our black hole re-positioning scheme, their “dynamics” is largely unaffected by the low resolution contamination; therefore, the merger rates are also not impacted by the presence of low resolution DM particles. We verified these by re-running simulations where the seeding is additionally restricted to halos with a maximum low resolution contamination  $< 1\%$ ; we find that this additional criterion does not significantly impact the rates of seeding and merger events.

### 3.1.3 Nomenclature for the zoom simulation runs

Here we briefly describe the nomenclature we use to hereafter (in Figure legends and captions) identify the different boxes amongst the large suite of simulations described throughout Section 3.

The general structure of our label is represented as “**L\*<sub>SM</sub>\*<sub>FOF</sub>\***” wherein each “**\***” following “**L**”, “**SM**” and “**FOF**” is replaced by the numerical value of  $L_{\max}$ ,  $\tilde{M}_{sf,mp}$  and  $\tilde{M}_h$  respectively. The value of  $M_{seed}$  is explicitly stated along with the label. As an example, the zoom run with  $L_{\max} = 10$ ,  $M_{seed} = 1 \times 10^5 M_{\odot}/h$ ,  $\tilde{M}_{sf,mp} = 50$ , and  $\tilde{M}_h = 3 \times 10^3$  is labelled as “**L10\_SM50\_FOF3000**” with  $M_{seed} = 1 \times 10^5 M_{\odot}/h$ .

## 3.2 Uniform volume simulation suite

In order to validate the gas-based seed models, our first step is to compare our seed model predictions with observations. To reliably compare with the volume-independent constraints of

<sup>1</sup> The peak height  $\nu$  of a halo quantifies the “extremeness” of the corresponding region in terms of its overdensity. It is defined as  $\nu \equiv \delta_c / \sigma(R, z)$  where  $\sigma^2(R, z)$  is the variance of the overdensity in a sphere of lagrangian radius  $R$  of the halo, specified by a spherical top hat window function as the weighing kernel.  $\delta_c = 1.686$  is the critical overdensity for a spherically symmetric collapse in an Einstein De-Sitter universe. Please refer to [Tinker et al. \(2008\)](#) for more details.

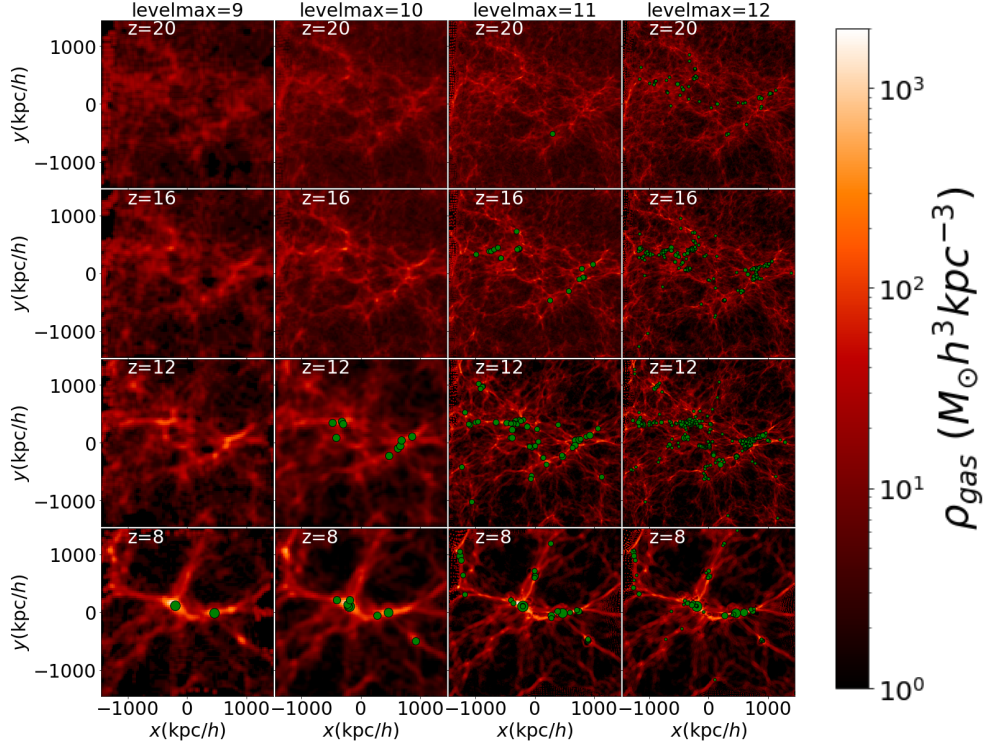


**Figure 1.** 2D color map of the gas density projection in ZOOM\_REGION\_z5 ( $3000 \times 3000 \times 50$  kpc/h). Left to right panels correspond to increasing resolution. Top to bottom panels show the redshift evolution from  $z = 20$  to  $z = 8$ . The green circles represent BHs (bigger circles are more massive BHs). Here, we show simulations where the seed masses are close to gas mass resolution. Therefore  $L_{\max} = 9, 10, 11, 12$  correspond to  $M_{\text{seed}} = 8 \times 10^5, 1 \times 10^5, 1.25 \times 10^4, 1.56 \times 10^3 M_{\odot}/h$  respectively. As the resolution increases, the simulations reveal finer structures that are able to capture the formation of lower-mass seed black holes at increasingly earlier epochs.

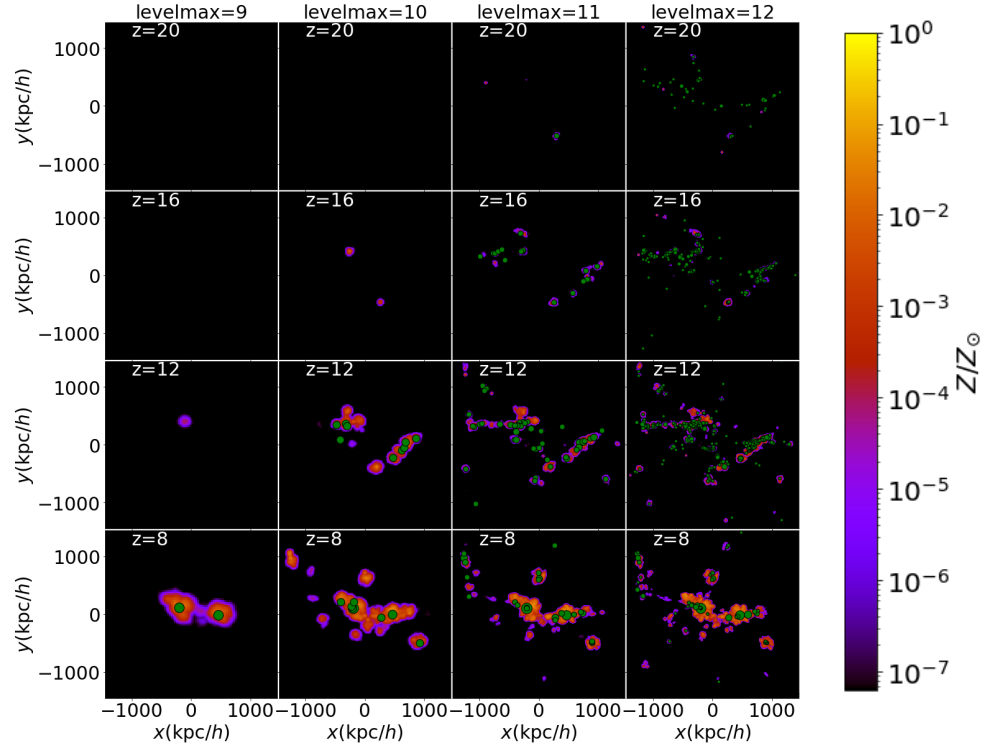


**Figure 2.** 2D color map of the gas metallicity projection in ZOOM\_REGION\_z5 ( $3000 \times 3000 \times 50$  kpc/h), for the same simulation snapshots as in Figure 1. As the resolution increases, the onset of star formation and metal enrichment happen at earlier epochs. However, the star formation and metal enrichment begin to approach convergence at  $L_{\max} \geq 11$ .

the luminosity functions and black hole mass functions, our predictions should have sufficiently low cosmic variance. Our zoom simulation predictions inevitably have a large cosmic variance due to their small volumes. Furthermore, the shape of the zoom volume becomes complex at late times due to its gravitational collapse, further complicating efforts to obtain volume-independent predictions from zoom simulations. For these reasons, we run a set of three uniform volume simulations with 25 Mpc/h box-size and  $512^3$  particles (using the same initial condition). The models for these uniform boxes are described as follows:

- The first and second boxes use the gas-based seed models (see Section 2.1). Both the boxes have  $M_{\text{seed}} = 8 \times 10^5 M_{\odot}/h$  and  $\tilde{M}_h = 3 \times 10^3$ .  $\tilde{M}_{\text{sf,mp}}$  is chosen to be 5 (referred as UNIFORM\_SM5) and 50 (referred as UNIFORM\_SM50) for the first and second box respectively.
- The third box (referred as UNIFORM\_FOF) uses the default halo mass based seed model from the Illustris-TNG suite. More specifically, seeds of  $M_{\text{seed}} = 8 \times 10^5 M_{\odot}/h$  are placed in halos above a mass of  $5 \times 10^{10} M_{\odot}/h$ . Hereafter, we shall also refer to this as the ‘TNG model’.

#### 4 COMPARISON WITH OBSERVATIONAL CONSTRAINTS

In this section, we use the uniform volume simulation suite (described in Section 3.2) to compare and validate our gas-based seed models against existing observational constraints. In Figure 3, we compare our model predictions of black hole masses to that of the observed black holes in the local Universe. The left panel shows the local ( $z = 0$ ) black hole mass functions predicted by our uniform boxes and compares it to  $z \sim 0$  observational constraints (Marconi et al. 2004; Shankar et al. 2004; Ferrarese & Ford 2005; Tundo et al. 2007; Merloni & Heinz 2008; Shankar 2013; Mutlu-Pakdil et al. 2016). We find that all three (UNIFORM\_SM5, UNIFORM\_SM50, UNIFORM\_FOF) models produce remarkable agreement with the observed measurements at  $M_{bh} \gtrsim 10^7 M_{\odot}/h$ . At  $10^6 \lesssim M_{bh} \lesssim 10^7 M_{\odot}/h$ , the UNIFORM\_SM50 and UNIFORM\_FOF models fully agree with the measurements but the UNIFORM\_SM5 model produces slightly higher number of black holes compared to the observations. However, this difference ( $\sim 0.7$  dex) may be difficult to be distinguishable given the observational uncertainties ( $\sim 0.5$  dex, see Figure 6 of Marconi et al. 2004).

The right panel of Figure 3 compares the model predictions for local  $M_* - M_{bh}$  relations to measurements from Magorrian et al. (1998), Reines & Volonteri (2015) & Terzazas et al. (2016). We find that the predictions for all the uniform boxes are broadly consistent with the measurements at  $M_{bh} \gtrsim 10^7 M_{\odot}/h$  living in galaxies with  $M_* \gtrsim 10^{10} M_{\odot}/h$ . For lower-mass black holes and galaxies, our models predict slightly higher black hole masses compared to the measurements. Additionally, at the highest mass end ( $M_* \sim 10^{12} M_{\odot}/h$  galaxies), simulations seem to mildly underpredict the black hole masses; however, we also expect a significant amount of cosmic variance at the most massive end due to our limited box size. Note that these differences between simulations and observations are also present for the TNG model, as also pointed out in Habouzit et al. (2020); but it is nevertheless encouraging to see that our gas-based seed

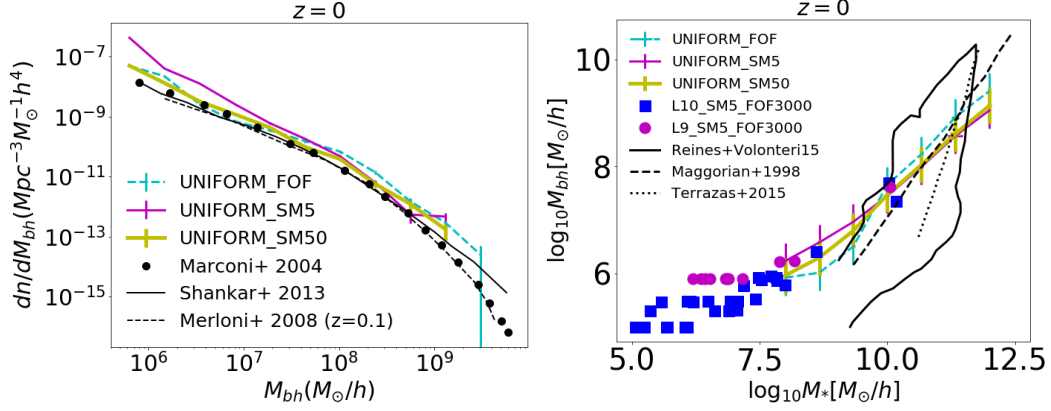
models produce local SMBH populations that are in good agreement with the TNG model. This also suggests that the local SMBH population is relatively insensitive to the seed models for black hole masses  $\gtrsim 10^6 M_{\odot}/h$ ; in this regime, differences between theory vs. observations likely point towards other aspects of the black hole models such as accretion and feedback. Notably, these results are overall consistent with Volonteri et al. (2008) which finds that for the local black hole population, differences between seed model predictions persist only at the low mass end ( $\lesssim 10^6 M_{\odot}/h$ ) of the black hole mass function. In addition to the uniform volume boxes, we also make predictions for zoom simulations for the region “ZOOM\_REGION\_z0” (see Section 3.1.2). The target galaxy in this zoom region has a mass of  $\sim 10^{10} M_{\odot}/h$  (see the most massive galaxy in Figure 3: right panel). We ran L9\_SM5\_FOF3000 with  $M_{\text{seed}} = 8 \times 10^5 M_{\odot}/h$  and L10\_SM5\_FOF3000 with  $M_{\text{seed}} = 1 \times 10^5 M_{\odot}/h$ , and find that both of them produce an SMBH of mass  $3 \times 10^7 M_{\odot}/h$  in the target galaxy; this is also consistent with the observed measurements.

Figure 4 shows the bolometric luminosity functions of the uniform volumes, compared with observed luminosity functions at  $z \sim 0 - 6$ . (Hopkins et al. 2007; Lacy et al. 2015; Shen et al. 2020). All of the uniform volume simulations produce similar luminosity functions, at least at the high-luminosity end. At high redshifts ( $z \gtrsim 2$ ), the differences between model predictions start to become distinguishable at  $\lesssim 10^{42} - 10^{43}$  ergs/s. These luminosities shall be accessible with upcoming X-ray facilities (e.g. Lynx; Schirra et al. 2020).

Next, we focus on comparing the model predictions to observational constraints in Figure 4. Note in general that the overlapping regime between the simulation predictions and the observed measurements is small. But in regimes where they do overlap, the simulation predictions are broadly consistent with the measurements of Lacy et al. (2015) at  $z \sim 0.2 - 1$ . We also find that the bright ends of the predicted luminosity functions are (when extrapolated) consistent with the bright ends of the observations at all redshifts between 0.2–6. However, there are some differences too between the measurements and our predictions. In particular, the measurements of Hopkins et al. (2007) and Shen et al. (2020) indicate a flattening of the slope at their faint end at  $\sim 10^{45}$  ergs/s. But the slope predicted by the simulations does not flatten until much lower luminosities ( $\sim 10^{43}$  ergs/s). In fact, the slopes for the simulation predictions at  $\sim 10^{43-45}$  ergs/s continue to be similar to those of the measurements at the brightest end ( $\sim 10^{45} - 10^{47}$  ergs/s). As a result, the simulations predict significantly higher numbers of AGN between  $\sim 10^{41} - 10^{45}$  ergs/s compared to Hopkins et al. (2007) and Shen et al. (2020).

The tension between the simulation vs observed luminosity functions has also been noted earlier by Weinberger et al. (2018), when comparing the predictions from IllustrisTNG. As noted in their work, there are a number of sources of uncertainty which can affect both the simulation predictions and observed measurements at the low luminosity end. For example, the simulation predictions depend sensitively on the radiative efficiency at low Eddington ratios; this may be different from the constant value of 0.2 as assumed by us (for instance, in general relativistic MHD simulations of accretion flows in Sadowski & Gaspari 2017, the radiative output in-





**Figure 3.** BH mass functions (left panel) and  $M_* - M_{bh}$  (right panel) relations at  $z = 0$ . In the right panels,  $M_*$  and  $M_{bh}$  correspond to the total stellar mass and black hole mass of subhalos (we only include subhalos with  $> 10$  particles; also true for subsequent figures). The solid pink and light green lines correspond to uniform volume simulations using gas-based seed models ( $\tilde{M}_h = 3 \times 10^3$ ) with  $\tilde{M}_{sf,mp} = 5$  (UNIFORM\_SM5) and 50 (UNIFORM\_SM50) respectively with  $M_{seed} = 8 \times 10^5 M_\odot/h$ . In the right panel, we also have pink and blue squares which are predictions from zoom simulations (ZOOM\_REGION\_z0 with  $\tilde{M}_h = 3 \times 10^3$ ,  $\tilde{M}_{sf,mp} = 5$ ) with  $L_{max} = 9$  (L9\_SM5\_FOF3000 with  $M_{seed} = 8 \times 10^5 M_\odot/h$ ) and 10 (L10\_SM5\_FOF3000 with  $M_{seed} = 1 \times 10^5 M_\odot/h$ ) respectively. The dashed cyan line corresponds to the default halo mass based seed model (UNIFORM\_FOF) used in IllustrisTNG. The black points and solid line (left panel) are observational measurements of the local black hole mass function from Marconi et al. (2004) and Shankar (2013) respectively; these are also consistent with other local measurements (for e.g. Shankar et al. 2004; Ferrarese & Ford 2005; Tundo et al. 2007; Shankar 2013; Mutlu-Pakdil et al. 2016) for black holes  $\gtrsim 10^7 M_\odot$  (see Fig. 5 of Shankar et al. 2009 and Fig. 13 of Mutlu-Pakdil et al. 2016). The black dashed line in the left panel is the constraint from Merloni & Heinz (2008) at  $z = 0.1$ . The black solid line (right panel) corresponds to the approximate outline for the observational scatter from Reines & Volonteri (2015). Black dashed and dotted lines (right panel) are mean stellar bulge mass vs. black hole mass relations from Magorrian et al. (1998) and Terrazas et al. (2016) respectively. The error-bars in the left panel are Poisson errors. The error-bars in the right panel are obtained via bootstrap resampling. Given the observational uncertainties, the measurements are broadly consistent with the simulation predictions.

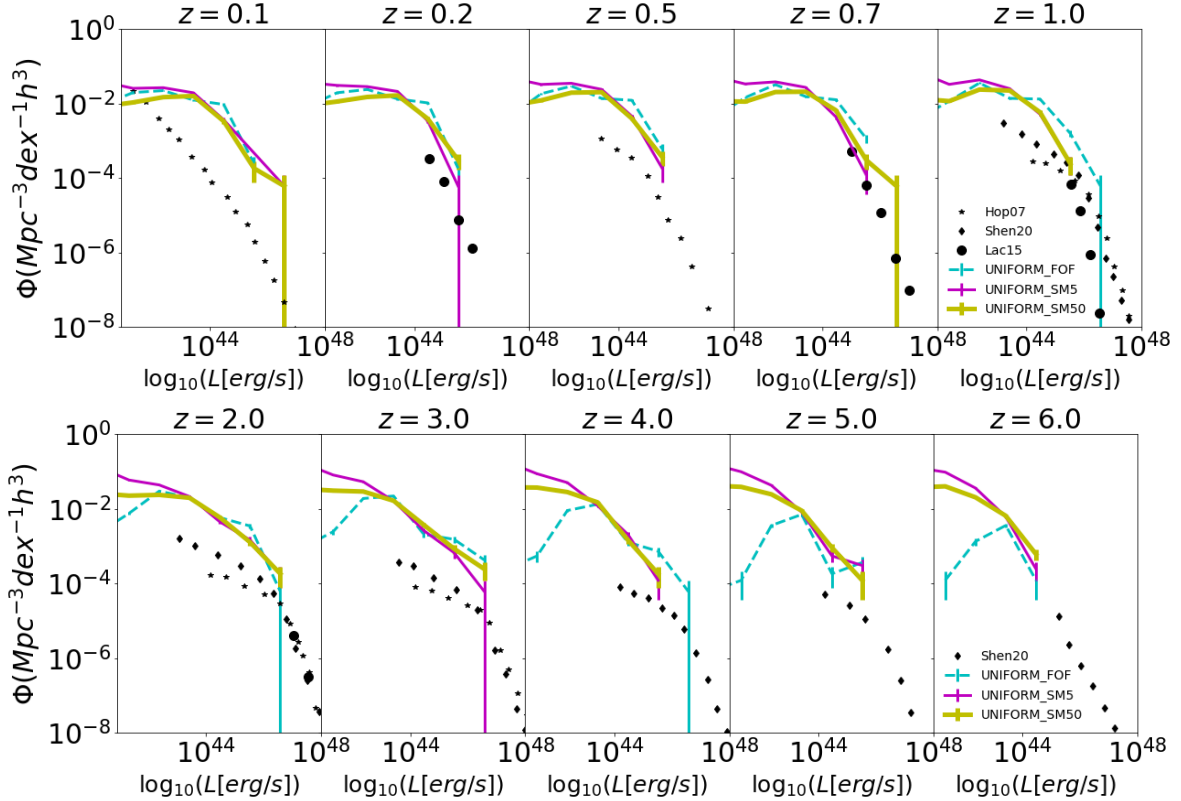


**Figure 4.** Luminosity functions between  $0.1 < z < 6$  for a set of uniform volume simulations. The solid pink and light green lines correspond to gas-based seed models ( $\tilde{M}_h = 3 \times 10^3$ ) with  $\tilde{M}_{sf,mp} = 5$  (UNIFORM\_SM5) and 50 (UNIFORM\_SM50) respectively. The dashed cyan line corresponds to the default halo mass based seed model (UNIFORM\_FOF) used in IllustrisTNG. The error-bars are Poisson errors. The black points correspond to observational constraints from (Hopkins et al. 2007, Hop07), (Lacy et al. 2015, Lac15) and (Shen et al. 2020, Shen20). Across all redshifts, the luminosity functions predicted by the gas-based seed models are consistent with the TNG model, particularly in the regimes probed by both simulations and observations.

creases with increase in Eddington ratio from  $10^{-6}$  to  $10^{-2}$ . At higher redshifts in particular, the discrepancies can also be potentially alleviated by a more efficient stellar feedback, as proposed by [Grand et al. \(2017\)](#) to account for insufficient suppression of star formation in  $z \sim 2 - 3$  galaxies. At the same time, the observed luminosity functions are also uncertain, particularly the number of Compton thick AGN at low luminosities ([Buchner et al. 2015](#)). Furthermore, evidence of significant obscuration in  $\lesssim 10^{45}$  ergs/s AGN is also found in recent works of [Habouzit et al. \(2019\)](#) and [Schirra et al. \(2020\)](#). That being said, models for [Hopkins et al. \(2007\)](#) and [Shen et al. \(2020\)](#) do account for obscuration, despite which the tension persists. Future measurements will shed further light on the tension between the simulations and observations at the low luminosity end ( $\sim 10^{42} - 10^{45}$  ergs/s) of the observed luminosity functions. But it is nevertheless encouraging to see that the different seed models have similar predictions in this regime.

Overall, we find that our gas-based seed models produce  $z \sim 0$  SMBH and  $z \lesssim 7$  AGN populations that are fully consistent with the TNG model. As a result, they also do not severely conflict with existing observational constraints, particularly for the black hole masses at  $z \sim 0$ . However, differences do exist (for both gas-based as well as TNG models) between simulations and observations for the AGN luminosity functions. But these differences seem to be largely insensitive to the seed model, and therefore points to other aspects of the black hole modeling such as accretion and feedback. Exploring the space of feedback and accretion models to study their impact on the luminosity functions will be a subject of future work. Here, we shall continue to explore our gas-based seed models to systematically assess their impact on the  $z \geq 7$  SMBH population.

## 5 IMPACT OF SEED PARAMETERS ON THE $Z \geq 7$ SMBH POPULATION

We now investigate how our seed parameters  $M_{\text{seed}}$ ,  $\tilde{M}_{\text{sf,mp}}$  and  $\tilde{M}_{\text{h}}$  affect the various observable properties of our SMBH population at  $z \gtrsim 7$ .

### 5.1 BH seed formation times

We first look at how the rates of seed formation are impacted by changing  $M_{\text{seed}}$ ,  $\tilde{M}_{\text{sf,mp}}$  and  $\tilde{M}_{\text{h}}$ . Before we proceed, it is important to understand the potential interdependencies between our three seed parameters. We first emphasize that the seeding frequency in our model effectively depends only on halo mass and star-forming, metal poor gas mass threshold. These thresholds are scaled to the seed mass  $M_{\text{seed}}$ ; therefore, any impact of changing  $M_{\text{seed}}$  is a simple consequence of the commensurate change in the total halo mass and star-forming, metal poor gas mass threshold. Figure 5 shows the correlation between the total halo mass and star-forming, metal poor gas mass. Not surprisingly, halos with higher total mass typically have higher star forming, metal poor gas mass (particularly for halos at  $z \gtrsim 11$  when metal enrichment is not that prevalent). However, the scatter between the total halo mass and star forming, metal poor gas mass is

significant (up to  $\sim 2$  dex); this is large enough that increasing the star forming, metal poor gas mass threshold does not significantly impact the minimum total mass of halos that can form seeds. Additionally, at lower redshifts ( $z \lesssim 11$ ), increased metal enrichment in halos generally leads to decrease in the star forming, metal poor gas mass, whereas the total halo mass continues to increase. These considerations motivate us to independently study the impact of  $\tilde{M}_{\text{sf,mp}}$  and  $\tilde{M}_{\text{h}}$ ; as we shall see, varying  $\tilde{M}_{\text{sf,mp}}$  and  $\tilde{M}_{\text{h}}$  indeed leads to qualitatively distinct impacts on seed formation.

Figures 6, 7 and 8 show the distribution of seeding redshifts for variations in  $M_{\text{seed}}$ ,  $\tilde{M}_{\text{sf,mp}}$  and  $\tilde{M}_{\text{h}}$ , respectively, for ZOOM\_REGION\_z5. We find that the seeds first start to form at redshifts ranging from  $z \sim 15 - 25$  depending on the parameters. As the simulation evolves, the number of seeds continues to increase up to  $z \sim 11$ . This is largely driven by the onset of star formation. In all of the gas-based seed models, the distributions of seed formation times peak at  $z \sim 11$ ; between  $z \sim 11 \pm 0.76$ , we can have 10 – 1000 seeds formed depending on the seed parameters. At  $z \sim 7 - 11$  however, new seed formation begins to be suppressed by contamination of star-forming regions with metals. In contrast to these gas-based seed models, the TNG model (black lines in Figures 6–8) produces only two seeds by  $z = 7$ , both of which do not form until  $z \sim 9$ . This is due to the much higher halo mass threshold in the TNG model ( $5 \times 10^{10} M_{\odot}/h$ ) than in the gas-based models ( $\sim 10^6 - 10^9 M_{\odot}/h$ ).

The fact that our seed formation peaks at  $z \sim 11$  is broadly consistent with previous works using hydrodynamic simulations such as [Tremmel et al. \(2017\)](#) and [Dunn et al. \(2018\)](#) where seeding is limited to regions that are metal poor as well as star forming; note that both of these studies emulate seeding conditions for DCBHs. It is also instructive to compare with SAMs, which form a relatively larger body of the existing literature. [Devecchi et al. \(2012\)](#) studied high redshift black hole formation using seeding criteria consistent with NSC and Pop III channels. In their work, the NSC seeds were formed in star forming regions with  $10^{-5} \lesssim Z \lesssim 10^{-3} Z_{\odot}$ ; most of these seeds formed at  $z \sim 11$ , similar to our results. However, their Pop III seeds (which formed from Pop III stellar remnants  $\gtrsim 260 M_{\odot}$  and  $Z \lesssim 10^{-5} Z_{\odot}$ ) tend to mostly form at  $z \gtrsim 20$ , which is significantly earlier than our model predictions. Similar results are seen for the Pop III channels in [Lupi et al. \(2014\)](#) and [Banik et al. \(2019\)](#). Overall, we find that our typical seed formation times of  $z \sim 11$  are in reasonable agreement with previous works that emulate DCBH and NSC seeding conditions. However, works that emulate Pop III seeding conditions tend to produce seeds substantially earlier ( $z \gtrsim 20$ ). This is not surprising given that 1) our seed masses ( $10^3 - 10^5 M_{\odot}/h$ ) are significantly higher than expected values for Pop III seeds ( $\sim 10^2 M_{\odot}/h$ ), and 2) our galaxy formation model does not include the full set of physics necessary for an accurate modelling Pop III star formation in mini-halos (halo masses  $\lesssim 10^5 M_{\odot}/h$ ). In particular, we do not model the formation of molecular hydrogen and its associated cooling; due to this, gas is not allowed to effectively cool below temperatures  $\lesssim 10^4$  K in mini-halos. In future work, we shall explore galaxy formation models which do include these necessary physics, and push our simulation resolutions to fully resolve Pop III seeds. The remainder of this subsection focuses on how the overall rates of seed formation are impacted by  $M_{\text{seed}}$ ,  $\tilde{M}_{\text{sf,mp}}$  and  $\tilde{M}_{\text{h}}$ .

Figure 6 illustrates that, as expected, fewer seeds form when the seed mass is larger. This results directly from our choice to scale the halo and gas mass thresholds to the seed mass. At  $z \gtrsim 11$ , the number of seeds formed is roughly linearly proportional to the seed mass; i.e., a  $\sim 100$  times larger seed mass produces  $\sim 100$  times fewer seeds. A natural corollary to this is the fact that lower mass seeds start forming at earlier epochs. As we shall see, at the highest redshifts these trends are primarily driven by the impact of increasing the halo mass threshold. At slightly lower redshifts ( $z \sim 7 - 11$ ), the number of seeds formed in each snapshot begins to decline. In this regime, differences between  $M_{\text{seed}}$  models in Figure 6 are instead driven primarily by the impact of increasing the star-forming, metal-poor gas mass threshold. We see less variation in the number of seeds formed; i.e.,  $M_{\text{seed}} = 1 \times 10^5 M_{\odot}/h$  produces  $\sim 10$  times fewer seeds compared to  $M_{\text{seed}} = 1.56 \times 10^3 M_{\odot}/h$ . In the next two paragraphs, we shall disentangle the impacts of star forming, metal poor gas mass threshold and halo mass threshold on the number of seeding events.

Figure 7 illustrates how the threshold mass of star-forming, metal-poor gas impacts the seed formation redshifts, for  $\tilde{M}_{\text{sf,mp}} = 5, 50, \& 150$ . Let us first focus on  $M_{\text{seed}} = 1.25 \times 10^4 M_{\odot}/h$  (Figure 7: left panels). We can clearly see that higher values of  $\tilde{M}_{\text{sf,mp}}$  suppress seed formation, particularly at  $z \lesssim 15$ . The stronger suppression of seed formation at  $z \lesssim 15$  is largely driven by metal enrichment and dispersion (see also Figure 19). Higher redshifts mark the earliest epochs of star formation, such that almost all the star forming gas mass is still metal poor and the seeding is primarily governed by the total amount of star forming gas mass in halos (i.e.  $\tilde{M}_{\text{sf,mp}} \approx \tilde{M}_{\text{sf}}$ ). When  $\tilde{M}_{\text{sf,mp}}$  is scaled to a larger seed mass of  $M_{\text{seed}} = 1 \times 10^5 M_{\odot}/h$ , seed formation is more strongly suppressed (right panels of Figure 7). For example, at  $\tilde{M}_{\text{sf,mp}} = 5$ , the overall number of  $1 \times 10^5 M_{\odot}/h$  seeds are  $\sim 10$  times lower compared to  $1.25 \times 10^4 M_{\odot}/h$  seeds. At higher values of  $\tilde{M}_{\text{sf,mp}}$  ( $= 50, 150$ ), even fewer seeds are formed. Here too, we see hints of stronger suppression at  $z \lesssim 15$  (similar to  $1.25 \times 10^4 M_{\odot}/h$  seeds but with poorer statistics).

Lastly, we look at the impact of  $\tilde{M}_{\text{h}}$ , which is shown in Figure 8. For both  $M_{\text{seed}} = 1.25 \times 10^4 \& 1 \times 10^5 M_{\odot}/h$  (right & left panels respectively), we find that increasing  $\tilde{M}_{\text{h}}$  from  $10^3$  to  $10^4$  leads to nearly uniform suppression of the number of seeds by a factor  $\sim 10$  across the entire redshift range between  $z \sim 11 - 25$ . This is a straightforward consequence of the halo mass function, which also suppresses by  $\sim 10$  when the threshold mass is increased from  $10^3$  to  $10^4 M_{\text{seed}}$ . Equivalently, we can also say that at  $z \sim 11 - 25$ , the halo mass criterion dominates the seeding because it is much more stringent than the star forming, metal poor gas mass criterion. At  $z \sim 7 - 11$  however, the halo mass criterion has much less impact on seed formation. This is because by  $z \sim 11$ , most halos that satisfy the star-forming, metal-poor gas mass criterion also satisfy the total halo mass criterion.

Contrasting the impact of the halo mass threshold ( $\tilde{M}_{\text{h}}$ ) and star forming, metal poor gas mass threshold ( $\tilde{M}_{\text{sf,mp}}$ ), we see that the halo mass threshold uniformly impacts the seeding at  $z \sim 11 - 25$  but does not impact the seeding at  $z \sim 7 - 11$ . On the other hand, the star-forming, metal-poor gas mass threshold impacts the seeding at  $z \sim 7 - 15$  but not at  $z \sim 20 - 25$ . These distinct effects of  $\tilde{M}_{\text{sf,mp}}$  and  $\tilde{M}_{\text{h}}$  are

primarily driven by the relative rates of halo growth vs. star formation vs metal enrichment. At higher redshifts, it is the lack of sufficiently massive star forming halos that is the main barrier for seed formation; therefore,  $\tilde{M}_{\text{h}}$  has a significant impact. As we approach lower redshifts, the growth of star forming halos does trigger seed formation; however, this is soon accompanied by metal enrichment that ultimately halts the formation of new seeds; therefore,  $\tilde{M}_{\text{sf,mp}}$  starts to have a more significant impact at lower redshifts.

## 5.2 Growth of BHs: Mergers vs. Accretion

Following seed formation, a black hole can grow by merging with other BHs, or by accreting the surrounding gas. Here we investigate the relative contributions of mergers vs. accretion in fueling black hole growth; this is shown in Figure 9 (black points) for black holes at the  $z = 7$  snapshot of ZOOM\_REGION\_z5. We find that black holes predominantly grow via merging with other black holes at  $z \geq 7$  for all of the parameter values we explore in this work. This is likely because: 1) low mass black holes are not able to accrete significantly within the Bondi Hoyle prescription wherein the accretion rate is  $\propto M_{\text{bh}}^2$ , 2) most of the black holes form in regions where the gas densities are not yet high enough to significantly fuel black hole accretion. Additionally, it is important to note that the mergers are being facilitated by our repositioning scheme. A more realistic model for black hole dynamics can lead to dynamical delays and reduce (or at least postpone) the number of mergers; this can curb the overall amount of merger driven black hole growth. Even though this paper focuses on  $z \geq 7$ , it is instructive to see how mergers and accretion contribute to black hole growth at lower redshifts. This is also shown in Figure 9 (purple, green and red points) from  $z = 7$  to 0 for ZOOM\_REGION\_z0. We find that as we approach  $z \sim 0$ , accretion starts to have an increasingly significant contribution to the black hole growth for increasingly massive black holes. However, the contribution of mergers still continues to be dominant ( $\gtrsim 50\%$ ) even at  $z = 1$  for black holes with masses up to  $10^7 M_{\odot}/h$ .

We also note that there are alternate accretion models where the accretion rate scales differently with  $M_{\text{bh}}$ ; for example, in the gravitational torque driven accretion models (Hopkins & Quataert 2011; Anglés-Alcázar et al. 2017; Davé et al. 2019), the accretion rate scales as  $M_{\text{bh}}^{1/6}$ . In such models, the early black hole growth at low masses would be much more rapid compared to that of Bondi accretion. This would likely increase the contribution of accretion to black hole growth at  $z \geq 7$ .

## 5.3 BH masses

In this section, we investigate the masses of the SMBH populations produced by our seed models. Figure 10 shows the number of black holes at each redshift snapshot. Note again that we do not present volume independent quantities such as comoving number densities because the overall zoom volume is not very well defined and is distorted by gravitational collapse. Also, recall from Section 3.1.2 that we only include black holes within 1 Mpc/h from the center of mass of the zoom volume, to avoid regions contaminated with low resolution DM particles. In general, we see that there is a steady

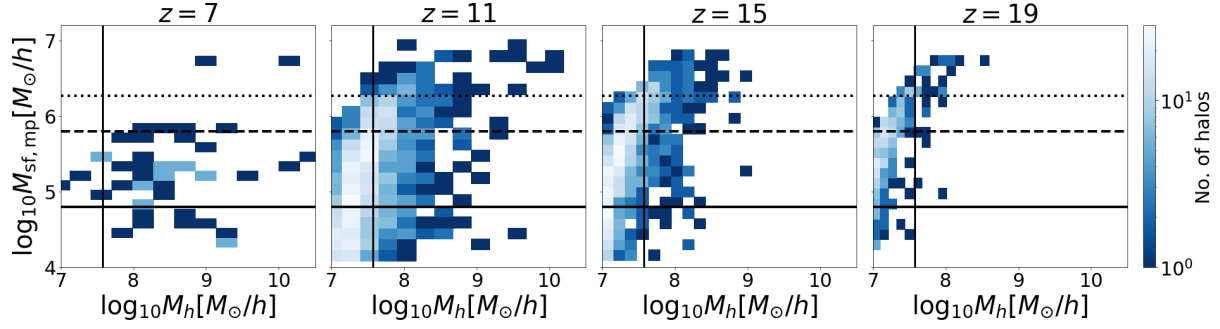


**Figure 5.** Blue histograms show the total halo mass ( $M_h$ ) vs star forming, metal poor gas mass ( $M_{\text{sf,mp}}$ ) for the halo populations at  $z = 7 - 19$  within ZOOM\_REGION\_z5. The following assumes  $M_{\text{seed}} = 1.25 \times 10^4 M_\odot/h$ . The vertical solid line corresponds to the seeding threshold of  $\tilde{M}_h = 3000$  for the total halo mass. The solid, dashed and dotted horizontal lines correspond to seeding thresholds of  $\tilde{M}_{\text{sf,mp}} = 5, 50$  and  $150$  for the star forming, metal poor gas mass. Generally, halos with higher total halo mass tend to have higher star forming, metal poor gas mass; however, there is significant scatter (up to  $\sim 2$  dex). As a result of the scatter, increasing  $\tilde{M}_{\text{sf,mp}}$  from 5 to 150 does not significantly impact the minimum total mass of halos in which seeds can form.

increase in the number of black holes up to  $z \sim 11$ , when black holes are rapidly forming and growing via mergers. At  $z \sim 7 - 11$  where seed formation begins to be suppressed by metal enrichment, merger events start to gradually decrease the number of black holes with time.

We now focus on how these results are impacted by  $M_{\text{seed}}$ . The leftmost panel of Figure 10 shows the overall number of BHs; not surprisingly, there is a significantly higher number of black holes produced by models with lower mass seeds. In particular,  $M_{\text{seed}} = 1.56 \times 10^3 M_\odot/h$  produces  $\sim 100$  times more black holes compared to  $M_{\text{seed}} = 1 \times 10^5 M_\odot/h$  at  $z \gtrsim 15$ ; at  $z \sim 7 - 11$ , the black hole counts for  $M_{\text{seed}} = 1.56 \times 10^3 M_\odot/h$  is 7–10 times higher than  $M_{\text{seed}} = 1 \times 10^5 M_\odot/h$ . We are also interested in the comparison of black hole counts above a minimum threshold mass for different  $M_{\text{seed}}$  (note that this minimum threshold mass is chosen to subsample the black hole populations, and is different from the intrinsic seed mass  $M_{\text{seed}}$  used during the simulation runs). The results of this comparison depend crucially on the relative growth rates of low mass vs high mass seeds. Above a mass threshold of  $2 \times 10^5 M_\odot/h$ ,  $M_{\text{seed}} = 1 \times 10^5 M_\odot/h$  produces  $\sim 3$  times more black holes for  $\tilde{M}_h = 10^3$ , compared to  $M_{\text{seed}} = 1.56 \times 10^3 M_\odot/h$ . The impact seems to be somewhat weaker for  $\tilde{M}_h = 3 \times 10^3$  (although that might also be partly due to fewer statistics). But overall, the impact of  $M_{\text{seed}}$  on black hole counts above a fixed mass threshold is relatively small. This is because lower mass seeds form earlier, which gives them enough time to grow (via mergers) and catch up with the higher mass seeds that form later.

We also note in Figure 10 that as the threshold mass increases to  $8 \times 10^5 M_\odot/h$  (rightmost panels), the black hole counts for the different  $M_{\text{seed}}$  models become indistinguishable (given the statistical uncertainties). Note also that these black holes are significantly larger than all the  $M_{\text{seed}}$  values that are being compared. To further explore the black hole abundances for even higher threshold masses, we show in Figure 11 the cumulative mass functions and  $M_{bh} - M_*$  relations at  $z = 7$ . We see that the black hole mass functions for the different models start to become similar for black holes  $\sim 3-4$  times heavier than the most massive seed; they continue to remain similar up to the most massive BHs ( $\sim 10^7 M_\odot/h$ ). We can even more clearly see this in the  $M_{bh} - M_*$  relations (Fig-

ure 11: right panels), wherein the most massive black holes have almost the same masses for models with different  $M_{\text{seed}}$ . This suggests that if seeds of different masses form in halos with commensurately different total mass and star forming, metal poor mass, they can grow into SMBHs with similar masses between  $\sim 10^6 - 10^7 M_\odot/h$  by  $z = 7$ .

$\tilde{M}_{\text{sf,mp}}$  and  $\tilde{M}_h$  have a more substantial impact (compared to  $M_{\text{seed}}$ ) at the massive end ( $\gtrsim 10^6 M_\odot/h$ ) of the cumulative mass functions and the  $M_* - M_{bh}$  relations (shown in Figures 12 and 13). At the most massive end, black hole masses are suppressed by factors of  $\sim 6$  when  $\tilde{M}_{\text{sf,mp}}$  is increased from 5–150. When  $\tilde{M}_h$  is increased by  $10^3 - 10^4$ , black hole masses are suppressed by factors of  $\sim 10$ . Additionally, the impact  $\tilde{M}_{\text{sf,mp}}$  and  $\tilde{M}_h$  on the mass functions are also qualitatively distinguishable. In particular, the impact of  $\tilde{M}_{\text{sf,mp}}$  on black hole abundances is largely uniform for the entire range of masses ( $\sim 10^4 - 10^7 M_\odot/h$ ) probed by these models. On the other hand, impact of  $\tilde{M}_h$  is somewhat stronger at the massive end of the black hole mass function (compared to the low mass end).

Lastly, we also compare our results with the TNG model, as applied to ZOOM\_REGION\_z5. These are shown as black lines / points throughout Figures 10 to 13. Recall from Section 5.1 that when this model is applied to our zoom region, only two halos produce black hole seeds ( $8 \times 10^5 M_\odot/h$ ) at  $z \sim 9$  (see Figures 6-8); they do not have any significant growth from  $z \sim 9$  to  $z \sim 7$ . We now look at the black hole masses produced in these two halos using the gas-based seed models. These correspond to the most massive black holes in the right panels of Figures 11, 12 and 13. We see that our gas-based seed models tend to produce black hole masses  $\sim 2-10$  times higher than the TNG model.

#### 5.4 Merger rates

In this section, we will quantify the impact of our seed model parameters on one of the most promising observable diagnostics of black hole seed models; i.e. black hole merger rates that could be probed with LISA. Before moving on, recall that two black holes are promptly merged when the distance between them is below the neighbor search radius of one of the black holes. Therefore, we are not able to probe the dy-



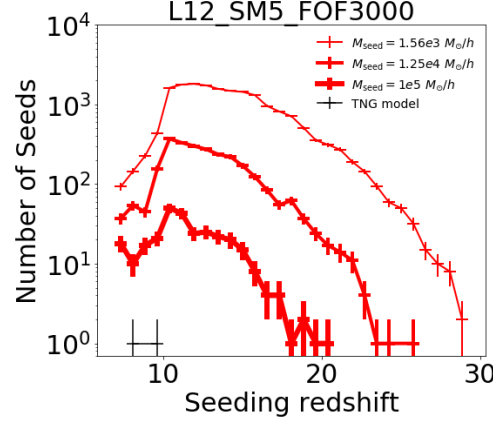


**Figure 6. Dependence of seed formation times on  $M_{\text{seed}}$ :** Distribution of seed formation times for models with different  $M_{\text{seed}}$  at fixed  $\tilde{M}_{\text{sf,mp}} = 5$  and  $\tilde{M}_h = 3 \times 10^3$  (for ZOOM\_REGION\_z5). The  $\tilde{M}_{\text{sf,mp}}$  and  $\tilde{M}_h$  values can be inferred from the label “L\*\_SM\*\_FOF\*”, wherein each “\*” following “L”, “SM” and “FOF” is replaced by the numerical value of  $L_{\text{max}}$ ,  $\tilde{M}_{\text{sf,mp}}$  and  $\tilde{M}_h$  respectively. The value of  $M_{\text{seed}}$  is explicitly stated along with the label. We adopt this convention to label our zoom boxes throughout the remaining figures of the paper. The error-bars in the number counts are Poisson errors (this is true for all the remaining figures which show number counts) These simulations are all run at  $L_{\text{max}} = 12$ . The distributions peak at  $z \sim 11$ . As  $M_{\text{seed}}$  increases, there is a delay in the onset of seeding and concurrently, the number of seeding events is suppressed at all redshifts.

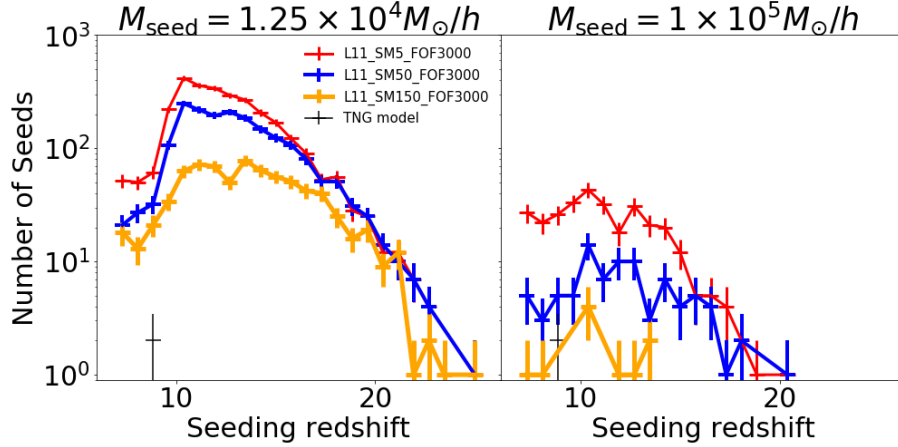


**Figure 7. Dependence of seed formation times on  $\tilde{M}_{\text{sf,mp}}$ :** Distribution of seed formation times for models with different star-forming, metal-poor gas mass thresholds  $\tilde{M}_{\text{sf,mp}}$  at fixed  $M_{\text{seed}}$  and  $\tilde{M}_h = 3 \times 10^3$  (for ZOOM\_REGION\_z5). These simulations are all run at  $L_{\text{max}} = 11$ . Left and right panels correspond to seed masses of  $M_{\text{seed}} = 1.25 \times 10^4 M_{\odot}/h$  and  $M_{\text{seed}} = 1 \times 10^5 M_{\odot}/h$ , respectively. As  $\tilde{M}_{\text{sf,mp}}$  is increased, seeding is suppressed largely at  $z \sim 7 - 15$ , with relatively little impact at  $z \gtrsim 15$ . Additionally, the impact of  $\tilde{M}_{\text{sf,mp}}$  is stronger for higher mass seeds.

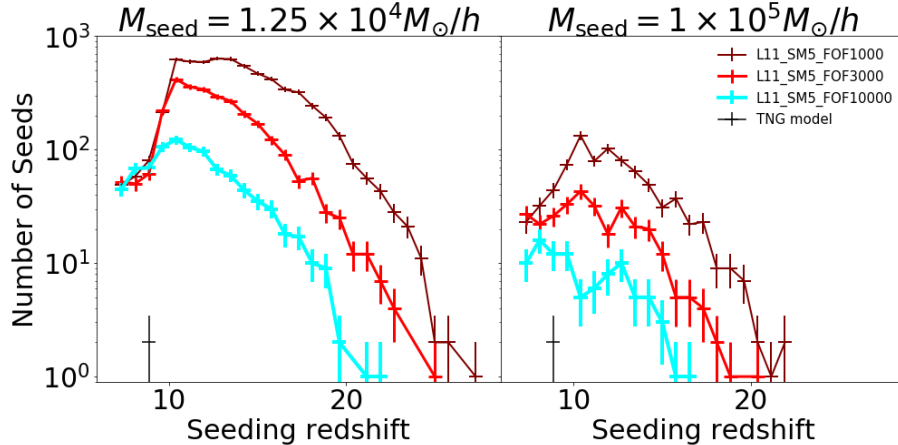


**Figure 8. Dependence of seed formation times on  $\tilde{M}_h$ :** Similar to Figure 7, but for different total halo mass thresholds  $\tilde{M}_h$  at fixed  $M_{\text{seed}}$  and  $\tilde{M}_{\text{sf,mp}} = 5$ . The distributions peak at  $z \sim 11$ . Increasing  $\tilde{M}_h$  uniformly suppresses the seeding throughout  $z \sim 11 - 25$ , but no significant suppression is seen at  $z \sim 11$ . The impact of  $\tilde{M}_h$  is similar for both seed masses.

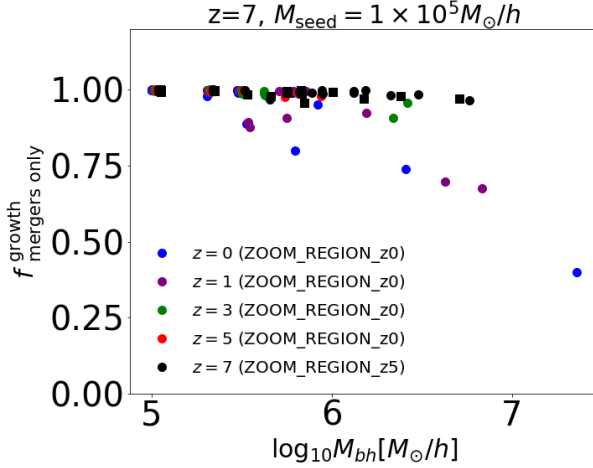


**Figure 9.**  $f_{\text{mergers only}}^{\text{growth}}$  is the fraction of mass that a black hole accumulates via mergers only. This is defined as  $f_{\text{mergers only}}^{\text{growth}} = (N_{\text{prog}} M_{\text{seed}}) / M_{\text{bh}}$  where  $N_{\text{prog}}$  is the number of progenitors of the black hole at a given snapshot. The black points show the results for the  $z = 7$  snapshot of ZOOM\_REGION\_z5 for models with  $\tilde{M}_{\text{sf,mp}} = 5, 50$  &  $150$  (circles, squares & stars respectively). At  $z \geq 7$ , the growth is almost completely driven by black hole mergers, since the accretion rates are small. The purple, green and red circles show the redshift evolution of  $f_{\text{mergers only}}^{\text{growth}}$  from  $z = 7$  to  $z = 0$  snapshot of ZOOM\_REGION\_z0 ( $\tilde{M}_{\text{sf,mp}} = 5$ ). This shows that as we move to lower redshifts, the gas accretion starts to become increasingly important for more massive black holes. However, mergers continue to remain the dominant contributor ( $\gtrsim 50\%$ ) to black hole growth for  $M_{\text{bh}} \sim 10^4 - 10^7 M_{\odot}/h$  even at  $z = 1$ .

namics and finite timescale for black hole mergers below the resolution limit of the simulation. This would inevitably impact our merger rate predictions depending on the time delay between the simulated merger event and the “actual merger event”. For example, if we assume a fixed time delay for every merger, our predicted merger rates would be higher than the “actual merger rate” (i.e. merger rates inferred after accounting for the time delay) at epochs when the merger rate is increasing with time; conversely, the predicted merger rates would be lower than the “actual merger rate” at epochs when the merger rate is decreasing with time. As discussed above, however, the complexity of zoom simulation volumes prevents us from making volume-independent merger rate predictions in any case. Thus, our primary focus here is the dependence of merger rates on different seed model parameters. The merger rates vs. redshift are shown in Figures 14–17. The merger rates tend to increase from  $z \gtrsim 15$  to  $z \sim 10$ ; they generally peak at around  $z \sim 10$ . From  $z \sim 10$  to  $z \sim 7$ , the merger rates start to gradually flatten and drop (as the seeding events start also to drop).

Figure 14 shows the impact of  $M_{\text{seed}}$  on the merger rates at fixed  $\tilde{M}_{\text{sf,mp}}$  and  $\tilde{M}_{\text{h}}$ . As expected, models with lower mass seeds tend to produce more mergers, largely because lower mass seeds are overall more numerous. More specifically,  $M_{\text{seed}} = 1.56 \times 10^3 M_{\odot}$  produces  $\sim 10$  times more mergers at  $z \sim 7$  and  $\sim 1000$  times more mergers at  $z \sim 15$ , compared to  $M_{\text{seed}} = 1 \times 10^5 M_{\odot}$ .

Next, we are interested in how the merger rates above a fixed black hole mass threshold vary with  $M_{\text{seed}}$ ; these are shown in Figure 15. We find that the rate of mergers be-

tween black holes above a fixed mass varies much less with  $M_{\text{seed}}$  than does the global merger rate. This is not very surprising given that the overall black hole counts above fixed mass thresholds (recall Figure 10) also show a similar amount of variation. We now take a closer look at different mass thresholds, starting with  $> 2 \times 10^4 M_{\odot}/h$  (Figure 15: left panels) black holes. Here, we can compare results for  $M_{\text{seed}} = 1.56 \times 10^3, 1.25 \times 10^4 M_{\odot}/h$ . For  $\tilde{M}_{\text{h}} = 1000$  (Figure 15: upper panels), there is generally a higher number of mergers (by factors up to  $\sim 3$ ) for  $M_{\text{seed}} = 1.25 \times 10^4 M_{\odot}/h$ , compared to  $M_{\text{seed}} = 1.56 \times 10^3 M_{\odot}/h$ . For mass thresholds of  $2 \times 10^5 M_{\odot}/h$  (Figure 15: right panels), we see similarly higher merger rates for  $M_{\text{seed}} = 1 \times 10^5 M_{\odot}/h$  compared to  $M_{\text{seed}} = 1.56 \times 10^3 M_{\odot}/h$  (albeit with fewer statistics). At higher  $\tilde{M}_{\text{h}} = 3000$  (Figure 15: lower panels), the variation with respect to  $M_{\text{seed}}$  seems to be slightly smaller.

Figure 16 shows how varying  $\tilde{M}_{\text{sf,mp}}$  for fixed  $M_{\text{seed}} = 1.25 \times 10^4 M_{\odot}/h$  and  $\tilde{M}_{\text{h}} = 3000$  impacts the overall merger rates. We can see that across the entire redshift range of  $z \sim 7 - 15$ , the merger rates are suppressed by factors of  $\sim 8$  when  $\tilde{M}_{\text{sf,mp}}$  is increased from 5 to 150. At  $z \gtrsim 15$ , variations in  $\tilde{M}_{\text{sf,mp}}$  have a slightly smaller effect on the merger rates. In stark contrast, Figure 17 demonstrates that the impact of  $\tilde{M}_{\text{h}}$  is stronger at higher redshifts. More specifically, at  $z \sim 7$  the merger rates are suppressed by factors of  $\sim 8$  when  $\tilde{M}_{\text{h}}$  is increased from  $10^3$  to  $10^4$ ; but the suppression is by factors  $\gtrsim 100$  for  $z \gtrsim 15$ .

Overall, we find that each of our model parameters have distinct imprints on the merger rates. First,  $M_{\text{seed}}$  naturally has the maximum impact on the merger rates amongst all the parameters, largely because it substantially increases the overall number of black holes. Next, the effects of  $\tilde{M}_{\text{h}}$  and  $\tilde{M}_{\text{sf,mp}}$  are dramatically different at different redshifts. The influence of  $\tilde{M}_{\text{sf,mp}}$  is relatively uniform whereas the impact of  $\tilde{M}_{\text{h}}$  is disproportionately stronger at higher redshifts. These distinctions are primarily governed by how our model parameters influence the seed formation times. These findings are useful in the context of LISA, which is expected to be able to detect  $\gtrsim 10^4 M_{\odot}/h$  black hole mergers all the way up to  $z \sim 15$ . In particular, they shall be useful for interpreting any potential tension that can occur between future measurements of LISA merger rates and simulation predictions. For example, if the tension in the simulated vs observed merger rates is substantial at  $z \gtrsim 15$ , this would hint that the typical halo masses for the seeds of the observed black holes are significantly different from the simulations. On the other hand, the simulated and observed merger rates may be similar at  $z \gtrsim 15$  but diverge at lower redshifts ( $z \sim 7 - 11$ ); this would hint that the seeds of observed black holes may have formed in halos with similar total mass, but different star forming, metal poor mass, compared to simulations.

Finally, we also note that TNG model (with  $M_{\text{seed}} = 8 \times 10^5 M_{\odot}/h$ ) does not produce any merger events at  $z \gtrsim 7$  within our zoom volume. Our gas-based seed models also produce only  $\sim 1 - 4$  mergers of  $> 8 \times 10^5 M_{\odot}/h$  black holes at  $z \gtrsim 7$ . Therefore the statistics are too limited to make any firm conclusions about the comparison of merger rate predictions for the TNG model vs gas-based seed prescriptions (above a fixed mass threshold of  $8 \times 10^5 M_{\odot}/h$ ).

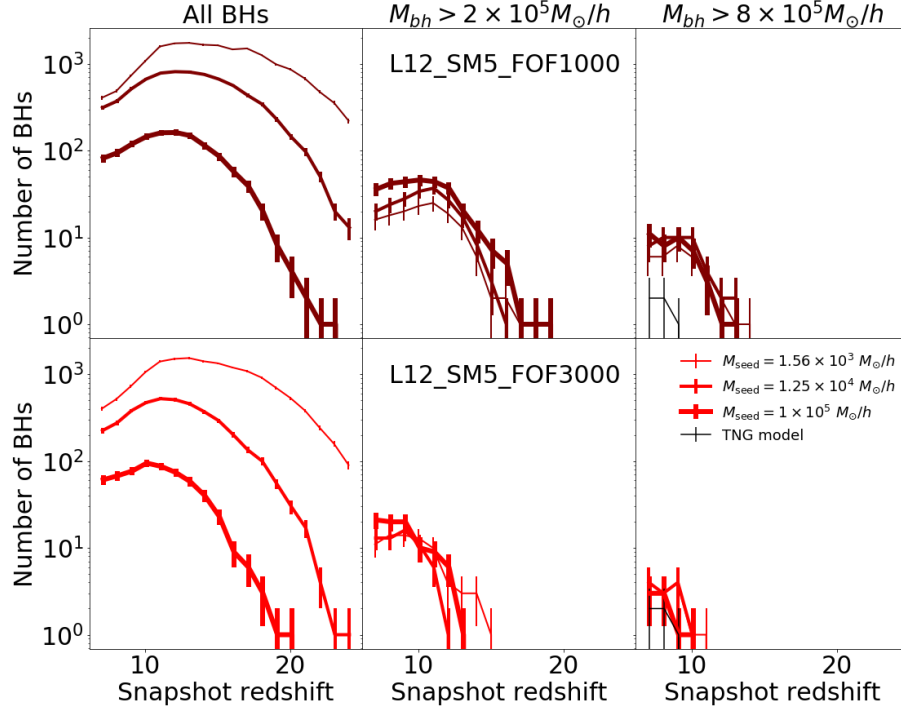


**Figure 10. Dependence of black hole count vs. redshift on  $M_{\text{seed}}$ :** Number of black holes as a function of redshift for models with different  $M_{\text{seed}}$  at fixed  $\tilde{M}_{\text{sf,mp}} = 5$  and  $\tilde{M}_h$  (in region ZOOM\_REGION\_z5). Leftmost panel correspond to all BHs; middle and right panels correspond to black holes above fixed mass thresholds of  $2 \times 10^5 M_\odot/h$  and  $8 \times 10^5 M_\odot/h$  respectively. Upper and lower panels correspond to  $\tilde{M}_h = 10^3$  and  $3 \times 10^3$  respectively. The black line in the 3rd panels corresponds to the TNG seed model applied to our zoom region. These are results for  $L_{\text{max}} = 12$ . Left to right panels correspond to increasing black hole mass thresholds. We find that the number of black holes is generally insensitive to  $M_{\text{seed}}$  (particularly at  $z \sim 7 - 10$ ) for mass thresholds substantially higher than the  $M_{\text{seed}}$  values.

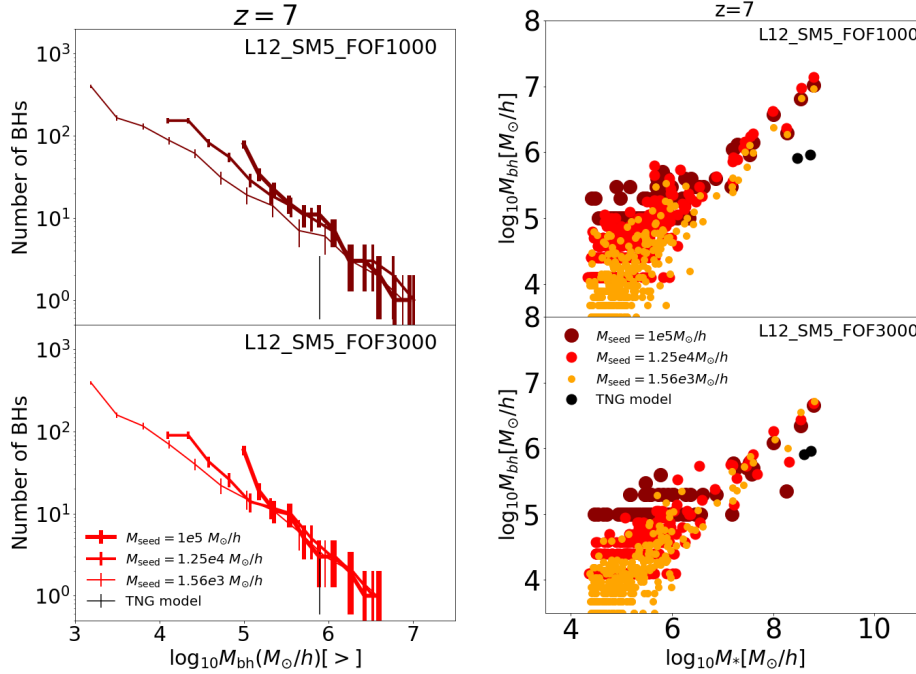


**Figure 11. Dependence of cumulative mass functions and  $M_{bh} - M_*$  relations on  $M_{\text{seed}}$ :** Left and right panels show the cumulative mass functions and  $M_{bh} - M_*$  relations for models with different  $M_{\text{seed}}$  at fixed  $\tilde{M}_{\text{sf,mp}} = 5$  and  $\tilde{M}_h$  (in region ZOOM\_REGION\_z5) at  $z = 7$ . In the right panels,  $M_*$  and  $M_{bh}$  correspond to the total stellar mass and black hole mass of subhalos. Upper and lower panels correspond to  $\tilde{M}_h = 10^3$  and  $3 \times 10^3$  respectively. Black color corresponds to the TNG model. We find that the massive end ( $\sim 3 \times 10^5 - 10^7 M_\odot/h$ ) of the black hole mass function and  $M_{bh} - M_*$  relation is insensitive to  $M_{\text{seed}}$ .

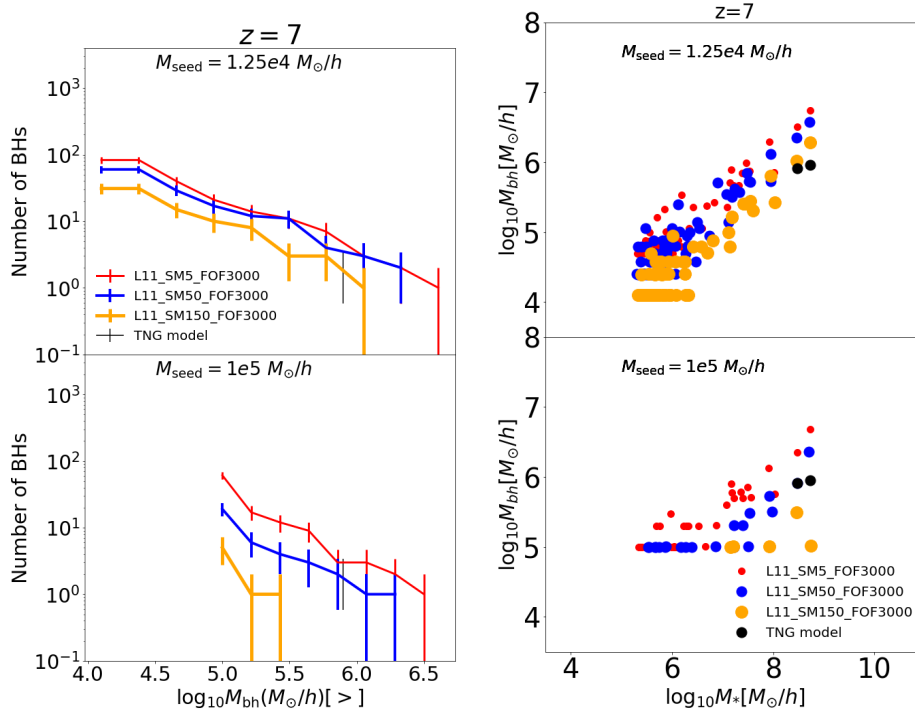


**Figure 12.** Dependence of cumulative mass functions and  $M_{bh} - M_*$  relations on  $\tilde{M}_{sf,mp}$ : Left and right panels show the cumulative mass functions and  $M_{bh} - M_*$  relations for models with different  $\tilde{M}_{sf,mp}$  at fixed  $M_{seed}$  and  $\tilde{M}_h = 3 \times 10^3$ . In the right panels,  $M_*$  and  $M_{bh}$  correspond to the total stellar mass and black hole mass of subhalos. Upper and lower panels correspond to  $M_{seed} = 1.25 \times 10^4 M_\odot/h$  and  $1 \times 10^5 M_\odot/h$  respectively. The black color corresponds to predictions from the TNG model. For the most massive black holes at  $z = 7$ , black hole masses are suppressed (by a factor of  $\sim 8$  for  $M_{seed} = 1.25 \times 10^4 M_\odot/h$ ) when  $\tilde{M}_{sf,mp}$  is increased (from 5 to 150). The suppression is stronger for higher seed masses.

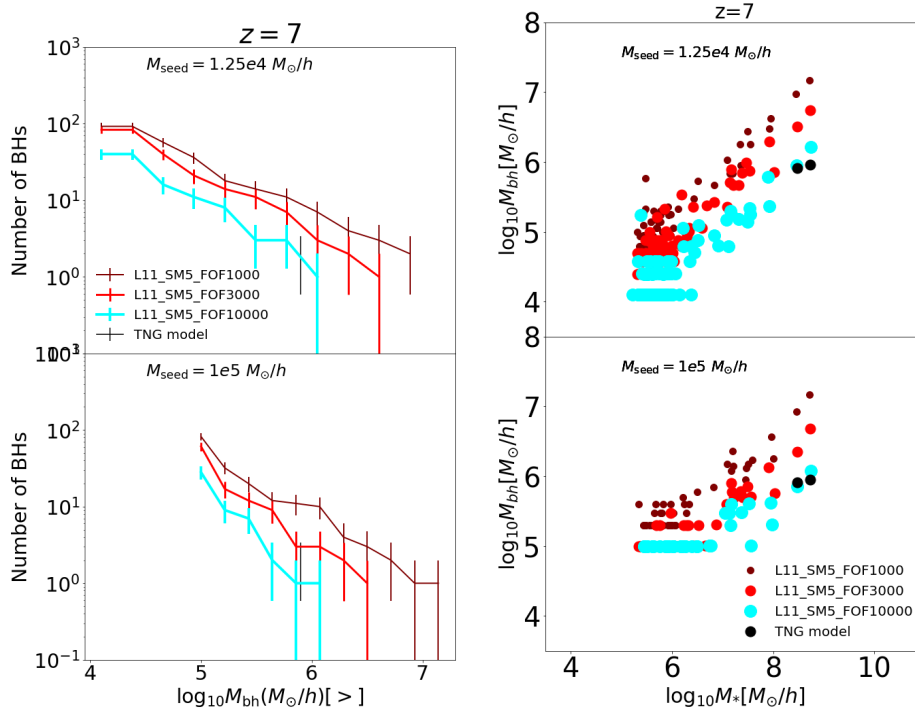


**Figure 13.** Dependence of cumulative mass functions and  $M_{bh} - M_*$  relations on  $\tilde{M}_h$ : Left and right panels show the cumulative mass functions and  $M_{bh} - M_*$  relations respectively for models with different  $\tilde{M}_h$  at fixed  $M_{seed}$  and  $\tilde{M}_{sf,mp} = 5$ . In the right panels,  $M_*$  and  $M_{bh}$  correspond to the total stellar mass and black hole mass of subhalos. Upper and lower panels correspond to  $M_{seed} = 1.25 \times 10^4 M_\odot/h$  and  $1 \times 10^5 M_\odot/h$  respectively. For the most massive black holes at  $z = 7$ , black hole masses are suppressed (by factors of  $\sim 10$ ) when  $\tilde{M}_h$  is increased (from  $10^3$  to  $10^4$ ). The suppression is similar for both seed masses.



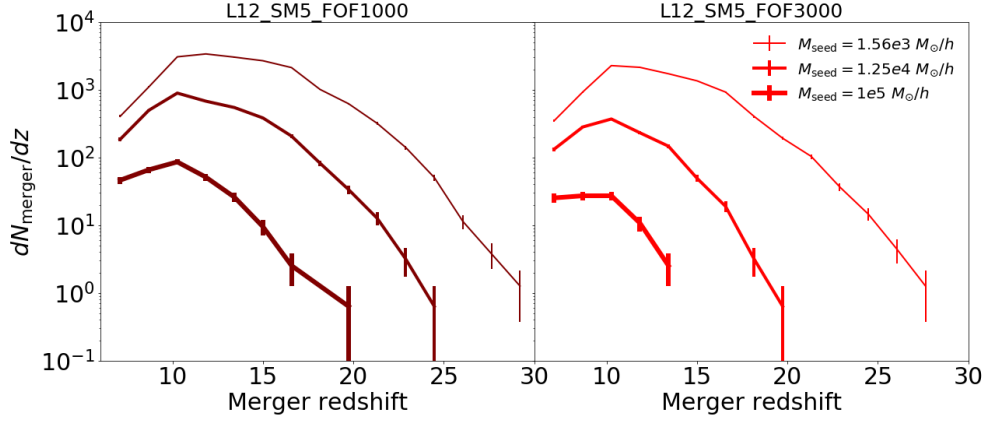


**Figure 14. Dependence of merger rates on  $M_{\text{seed}}$ :** Merger rates of all black holes for models with different  $M_{\text{seed}}$  at fixed  $\tilde{M}_{\text{sf,mp}} = 5$  and  $\tilde{M}_h = 3 \times 10^4$  (for ZOOM\_REGION\_z5). Left and right panels correspond to  $\tilde{M}_h = 10^3$  and  $3 \times 10^3$  respectively. These are all run at  $L_{\text{max}} = 12$ . Not surprisingly, lower mass seeds produce higher numbers of mergers.  $M_{\text{seed}} = 1.56 \times 10^3 M_{\odot}/h$  produces  $\sim 10$  times more mergers at  $z \sim 7$  and  $\sim 1000$  times more mergers at  $z \sim 15$ , compared to  $M_{\text{seed}} = 1 \times 10^5 M_{\odot}/h$ .

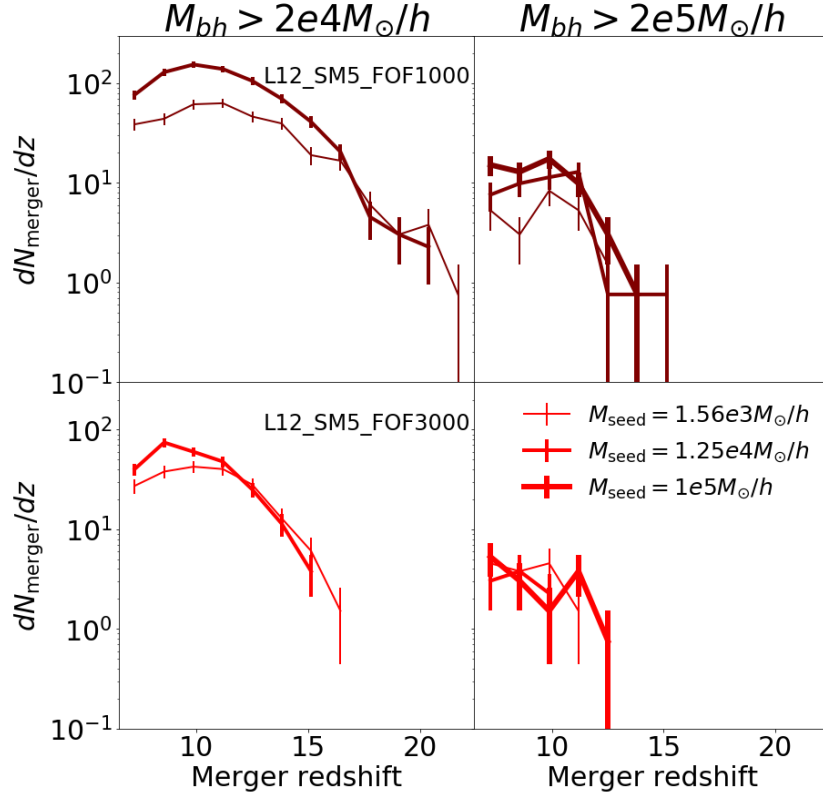


**Figure 15. Dependence of merger rates on  $M_{\text{seed}}$ :** Merger rates of black holes above fixed mass thresholds for models with different  $M_{\text{seed}}$  at fixed  $\tilde{M}_{\text{sf,mp}} = 5$  and  $\tilde{M}_h$  (for ZOOM\_REGION\_z5). Upper and lower panels correspond to  $\tilde{M}_h = 10^3$  and  $3 \times 10^3$  respectively. These are all run at  $L_{\text{max}} = 12$ . Here we show that when a black hole mass threshold is applied, the differences between the different  $M_{\text{seed}}$  values become substantially smaller (up to factors of  $\sim 2 - 3$ ), compared to Figure 14.

## 5.5 AGN luminosity functions

In this section, we focus our attention on the AGN luminosity functions shown in Figure 18 for ZOOM\_REGION\_z5. Here too (as with the black hole masses), black holes are confined to within 1 Mpc/h from the center of mass of the zoom volume to avoid regions contaminated with low resolution DM particles. We compute the bolometric luminosities of the black holes from their mass accretion rates using Eq. (4).

Our gas-based seed models produce AGN up to bolometric luminosities as high as  $\sim 10^{44}$  ergs/s. In comparison, the TNG model has two black holes at  $z = 7$  with luminosities of  $\sim 10^{42}$  ergs/s. However, these AGN are still 2-3 orders of magnitude fainter than the observed population of  $z > 6$  quasars. This is not unexpected given that the largest black holes that we form in ZOOM\_REGION\_z5 have masses ranging from  $\sim 10^6 - 10^7 M_{\odot}/h$  (depending on the seed model), which is  $\sim 10 - 100$  times smaller than the typical masses of the first

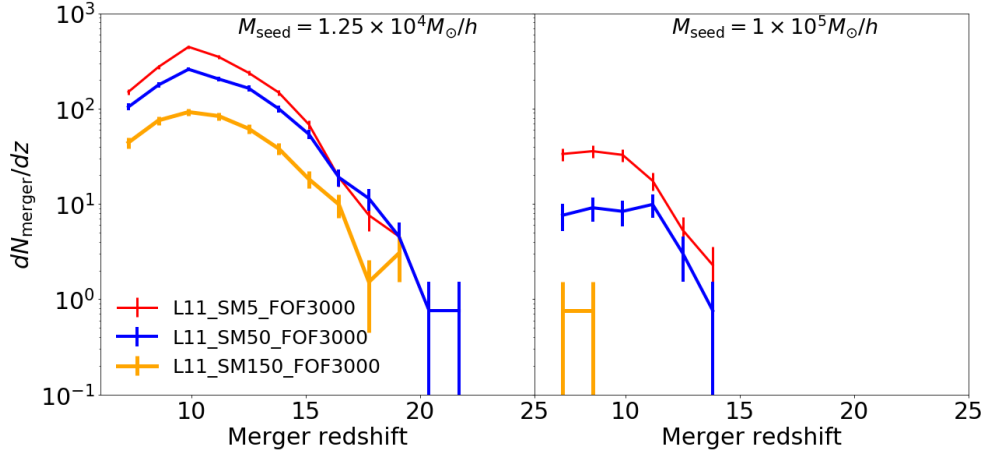


**Figure 16. Dependence of merger rates on  $\tilde{M}_{\text{sf,mp}}$ :** Merger rates of all black holes for models with different  $\tilde{M}_{\text{sf,mp}}$  at fixed  $M_{\text{seed}}$  and  $\tilde{M}_h$  (for ZOOM\_REGION\_z5,  $M_{\text{seed}} = 1.25 \times 10^4 M_{\odot}/h$ ). These are all run at  $L_{\text{max}} = 11$ . As we increase  $\tilde{M}_{\text{sf,mp}}$  from 5 to 150, the merger rates are suppressed by factors  $\sim 8$  for  $M_{\text{seed}} = 1.25 \times 10^4 M_{\odot}/h$ . The suppression is only slightly smaller at  $z \gtrsim 15$  compared to  $z \sim 7 - 11$ . Lastly, the suppression is stronger for higher mass seeds.

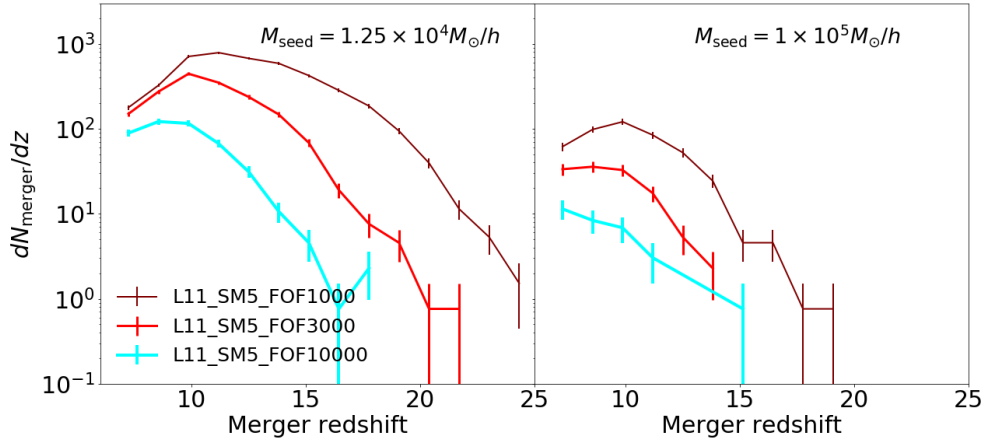


**Figure 17. Dependence of merger rates on  $\tilde{M}_h$ :** Merger rates of all black holes for models with different  $\tilde{M}_h$  at fixed  $\tilde{M}_{\text{sf,mp}}$  and  $M_{\text{seed}}$  (for ZOOM\_REGION\_z5,  $M_{\text{seed}} = 1.25 \times 10^4 M_{\odot}/h$ ). These are all run at  $L_{\text{max}} = 11$ . As we increase  $\tilde{M}_h$  from  $10^3$  to  $10^4$ , the merger rates have disproportionately larger suppression at higher redshifts. The suppression is by factors  $\gtrsim 100$  at  $z \gtrsim 15$ , whereas at  $z \sim 7 - 11$ , it is only by factors  $\sim 2 - 4$ .

quasars. More generally, ZOOM\_REGION\_z5 does not probe the observed high- $z$  quasar regime because it is selected from relatively small parent volume of  $(25 \text{ Mpc}/h)^3$ . In comparison, simulations that do successfully produce a few first quasars are  $\sim 4000$  times larger in volume (Tenneti et al. 2018; Ni et al. 2018; Marshall et al. 2020). Therefore, probing the observed high- $z$  quasar regime is beyond the scope of this paper, and we reserve this aspect for future work. The following paragraphs focus on the effect of our seed parameters on the luminosity functions.

We quantify the influence of our gas-based seed models at the detection limit of Lynx, which is assumed to be  $1 \times 10^{-19} \text{ ergs cm}^{-2} \text{ s}^{-1}$  in the  $2 - 10 \text{ keV}$  band for a survey area of  $360 \text{ arcmin}^2$  (Griffin et al. 2020). To convert this into a bolometric luminosity limit, we assume the bolometric correction derived in Vasudevan & Fabian (2007). We focus on Lynx because it is one of the only planned missions that is deep enough to potentially probe our simulated luminosities. The impact of  $M_{\text{seed}}$  on the luminosity functions is overall small compared to statistical uncertainties (Poisson errors)

in our predictions (see top panels of Figure 18). This is in fact true all the way down to  $10^{40} \text{ ergs/s}$ . Therefore, the differences in black hole abundances for models with different  $M_{\text{seed}}$  (seen in Figure 10) are largely contributed by very low luminosity ( $\lesssim 10^{40} \text{ ergs/s}$ ) black holes. The luminosity functions do vary somewhat with  $\tilde{M}_{\text{sf,mp}}$  and  $\tilde{M}_h$  (see middle and bottom panels of Figures 18). For  $M_{\text{seed}} = 1.25 \times 10^4 M_{\odot}/h$ , the luminosity functions at the Lynx limit are suppressed by factors of  $\sim 2 - 3$  from  $\tilde{M}_{\text{sf,mp}} = 5$  to 150. Varying  $\tilde{M}_h$  from  $10^3$  to  $10^4$  also suppresses the luminosity functions by factors of  $\sim 2 - 3$  at  $z = 7, 9$ . For higher seed masses (not shown in Figure 18), we report broadly similar trends but the statistical uncertainties are too high to make robust conclusions. Overall, while these variations are noteworthy, they are still relatively small (compared to the influence on merger rates, for instance). These variations are also somewhat smaller than the typical uncertainties in current measurements of high- $z$  luminosity functions ( $\sim 10 - 100 \text{ dex}$  at the faint end, see Figure 5 of Shen et al. 2020). Furthermore, the luminosity functions may also be influenced by other aspects of our

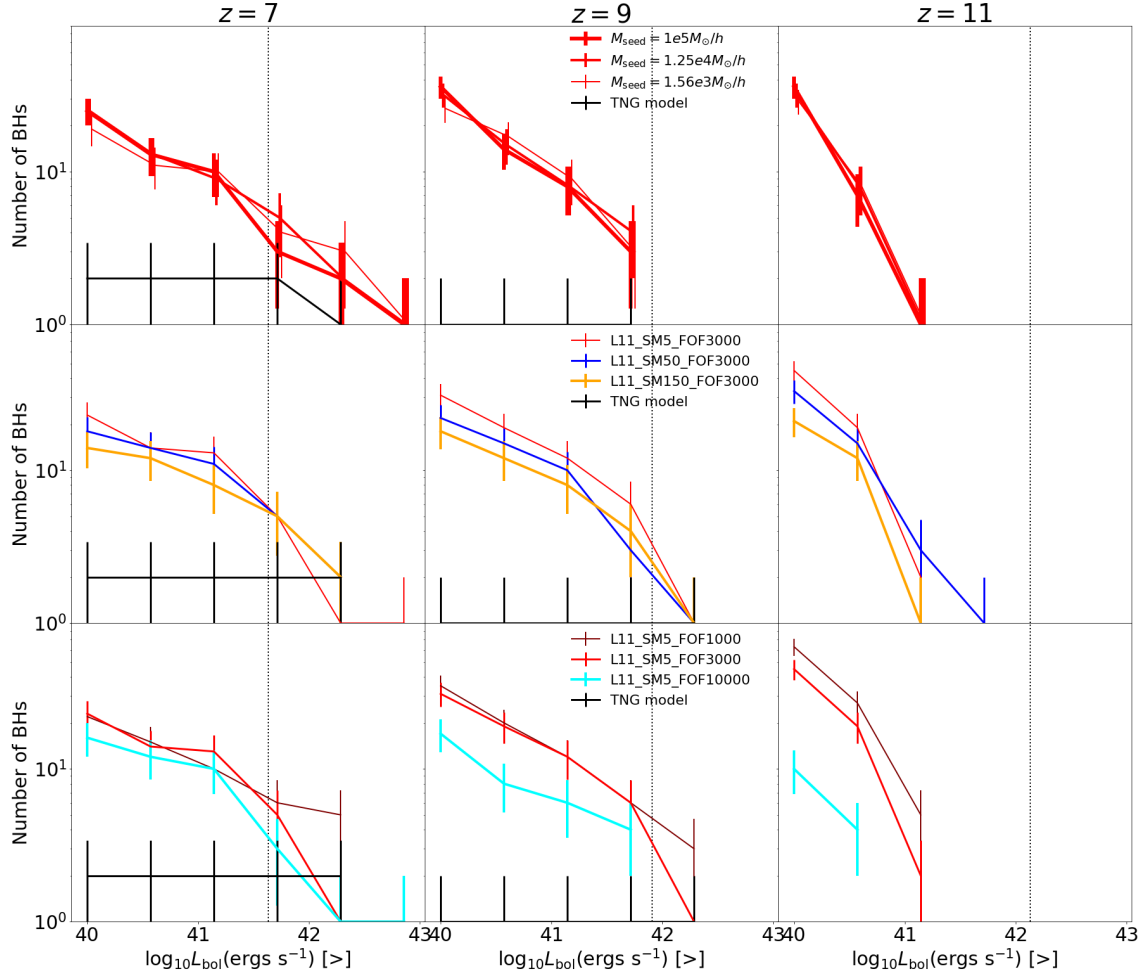


**Figure 18. Dependence of AGN luminosity functions on  $M_{\text{seed}}$ ,  $\tilde{M}_{\text{sf,mp}}$  and  $\tilde{M}_h$ :** Cumulative luminosity functions for different gas-based seed models as applied to ZOOM\_REGION\_z5. Upper panels correspond to models with different  $M_{\text{seed}}$  at fixed  $\tilde{M}_{\text{sf,mp}} = 5$  and  $\tilde{M}_h = 3000$ ; these are run at  $L_{\text{max}} = 12$ . Middle panels show models with different  $\tilde{M}_{\text{sf,mp}}$  at fixed  $M_{\text{seed}} = 1.25 \times 10^4 M_{\odot}/h$  and  $\tilde{M}_h = 3 \times 10^3$ . Lower panels correspond to different  $\tilde{M}_h$  at fixed  $M_{\text{seed}} = 1.25 \times 10^4 M_{\odot}/h$  and  $\tilde{M}_{\text{sf,mp}} = 5$ . The middle and lower panels are run at  $L_{\text{max}} = 11$ . The black line corresponds to the TNG model. Vertical lines correspond to the detection limit of Lynx, assumed to be  $1 \times 10^{-19} \text{ ergs cm}^{-2} \text{ s}^{-1}$  in the 2–10 keV band for a survey area of 360 arcmin<sup>2</sup> (Griffin et al. 2020). The required bolometric correction is adopted from Vasudevan & Fabian (2007). The variation in the luminosity functions is only up to factors of  $\sim 2-3$ ; therefore, it may be challenging for Lynx to be able to distinguish between these models.

model such as black hole accretion and feedback. Therefore, we suspect that it will be challenging for luminosity function constraints from future surveys such as JWST and Lynx to be able to distinguish between our seed models. We can put these results in context of prior work done using semi-analytic modeling. It is noteworthy that our conclusions somewhat differ from Ricarte & Natarajan (2018) who find that Lynx may be able to put constraints on seed models; however, this could be partly because their seeding and accretion prescriptions are widely different from ours. At the same time, Griffin et al. (2020) finds that the  $z \sim 7-12$  luminosity functions are not sensitive to their choice of seed masses ranging from  $10-10^5 M_{\odot}/h$ , consistent with our findings. In any case, recent work by Natarajan et al. (2017) hints that multi wavelength spectral observations from high- $z$  AGN and their host galaxies (using JWST) may have substantially higher constraining power compared to the overall bolometric luminosities (we plan to investigate this using our simulations in

a future study). This emphasizes the importance of continued work on finding electromagnetic signatures of black hole seeds.

## 6 RESOLUTION CONVERGENCE

In this section, we examine the resolution convergence of the results presented in this work. Recall that the black hole seeding essentially depends on the amount of star forming, metal poor gas mass in halos as well as total mass of the halos. The total halo mass is known to converge well even at significantly lower resolutions compared to our zoom regions (Lukić et al. 2007). Therefore, the resolution convergence of our final black hole populations is primarily driven by the resolution convergence of star formation and metal enrichment. We first revisit Figures 1 and 2 which show the density and metallicity evolution at different resolutions i.e.  $L_{\text{max}} = 9, 10, 11, 12$ . We see that with increasing  $L_{\text{max}}$ , we are able to resolve higher

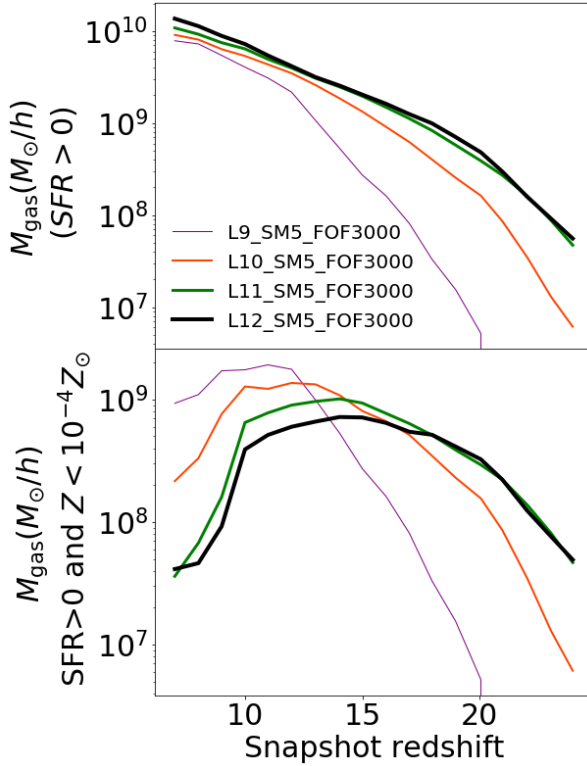


**Figure 19. Top Panel:** The evolution of the total mass of star forming gas over the entire ZOOM\_REGION\_z5 (for the same simulations as in Figures 1 and 2). The star formation evolution approaches convergence at  $L_{\text{max}} = 11, 12$ . **Bottom Panel:** The evolution of the total mass of star forming, metal poor ( $Z < 10^{-4} Z_{\odot}$ ) gas over the entire ZOOM\_REGION\_z5. Following the star formation, the metal enrichment evolution also approaches convergence at  $L_{\text{max}} = 11, 12$ . However, the convergence is slower at  $z \lesssim 17$ , wherein the  $L_{\text{max}} = 12$  still has a notably faster metal enrichment compared to  $L_{\text{max}} = 11$ . This can also be visually seen in Figure 2.

densities on smaller scales. This leads to earlier onset of star formation and metal enrichment at higher resolutions. This is easily seen in Figure 2 wherein for  $L_{\text{max}} = 11$  & 12, the first metal enriched regions appear before  $z = 20$ . In contrast, for  $L_{\text{max}} = 9$  & 10, the first metal enriched regions do not appear until after  $z = 20$ . However, as we shall quantitatively demonstrate in the remaining paragraphs, our black hole seed models are reasonably well converged by  $L_{\text{max}} \geq 11$ .

In Figure 19, we quantify the resolution convergence of star formation and metal enrichment by showing the evolution of the total star forming gas mass (top panel) and star forming, metal poor gas mass (bottom panel) of all gas cells in the zoom region at  $L_{\text{max}} = 9, 10, 11, 12$  (recall that metal poor gas cells are defined to have metallicity  $Z < 10^{-4} Z_{\odot}$ ). We can see that the increase in star forming gas mass happens earlier at higher resolutions between  $L_{\text{max}} = 9 - 11$ , but star formation is well converged at  $L_{\text{max}} = 11$  & 12.

The resolution convergence of metal enrichment can be seen in Figure 19 (bottom panel), where the star forming, metal poor gas mass starts to drop at  $z \lesssim 12 - 15$ . At higher  $L_{\text{max}}$ , the metal enrichment begins sooner, and the resulting drop in star forming, metal poor gas mass starts to occur at earlier redshifts. In particular, the drop occurs at  $z \sim 15$

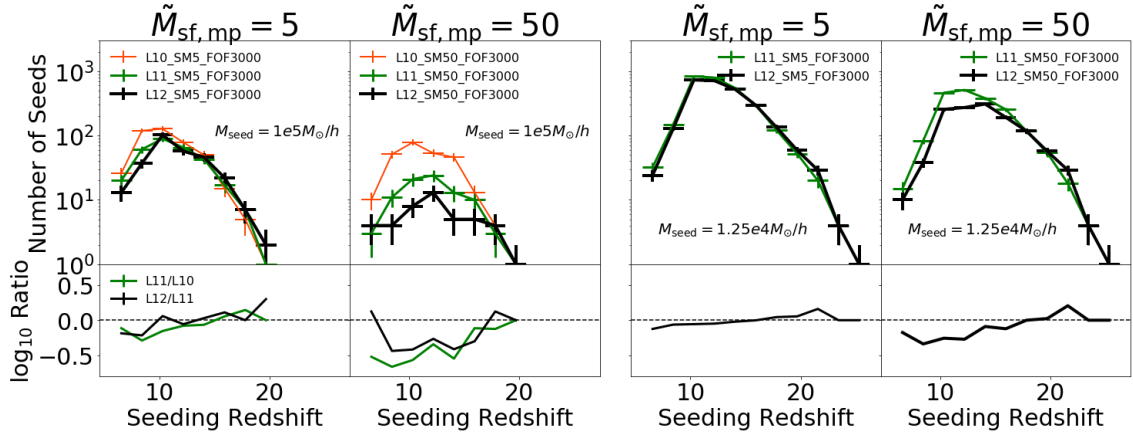
for  $L_{\text{max}} = 12$  and at  $z \sim 12$  for  $L_{\text{max}} = 9$ . Additionally, the drop also tends to become steeper at higher  $L_{\text{max}}$ ; this is an indicator of faster metal enrichment at higher  $L_{\text{max}}$ . At  $z \sim 7$ , the star forming, metal poor gas mass is  $\sim 30$  times lower for  $L_{\text{max}} = 11$  compared to  $L_{\text{max}} = 9$ . However, going from  $L_{\text{max}} = 11$  to  $L_{\text{max}} = 12$ , the decrease is only by a factor  $\sim 1.5$ . This is clear evidence that the metal enrichment exhibits resolution convergence. However, we do note the star forming, metal poor gas mass converges more slowly than the star forming gas mass. This implies that the convergence in metal enrichment is slower than that of star formation. We shall look at how this affects the convergence properties of black hole populations in the following paragraphs.

Figure 20 shows the distributions of seeding times (redshifts) at different resolutions. We are able to perform resolution convergence tests across  $L_{\text{max}} = 10 - 12$  for  $M_{\text{seed}} = 1 \times 10^5 M_{\odot}/h$ , and across  $L_{\text{max}} = 11 - 12$  for  $M_{\text{seed}} = 1.25 \times 10^4 M_{\odot}$ . Let us start with  $\tilde{M}_{\text{sf,mp}} = 5$ . At  $M_{\text{seed}} = 1 \times 10^5 M_{\odot}$ , we find that differences in the distributions between successive values of  $L_{\text{max}}$ , becomes smaller at higher resolutions (see lower panel of 1st column); between  $L_{\text{max}} = 11, 12$ , the agreement is to within  $\sim 25\%$  at  $z \gtrsim 10$ . At  $M_{\text{seed}} = 1.25 \times 10^4 M_{\odot}/h$ , we find even better agreement ( $\lesssim 10\%$ ) between  $L_{\text{max}} = 11, 12$ . These are overall strong signatures of resolution convergence. At  $z \sim 7 - 11$  however, the convergence is weaker and the number of seeds differs by factors  $\sim 2$  between  $L_{\text{max}} = 12$  vs. 11. Notice also that at  $z \lesssim 11$ , the formation of new seeds begins to slow down as halos become increasingly metal-enriched. This strongly suggests that the weaker resolution convergence at  $z \sim 7 - 11$  is driven by the onset of metal enrichment (and the fact the metal enrichment converges more slowly than star formation).

If we increase  $\tilde{M}_{\text{sf,mp}}$  to 50 (see again Figure 20: 2nd and 4th columns panels), the differences between  $L_{\text{max}} = 10, 11, 12$  start to appear even earlier ( $z \lesssim 15$ ), and the level of convergence is poorer. This reflects the earlier onset of metal enrichment in the higher-resolution runs, which places more stringent constraints on seed formation sites when a larger reservoir of star-forming, metal-poor gas is required. Overall, despite the varying rates of convergence for different parameter values, the important finding here is that our rates of seed formation indeed exhibit resolution convergence. Since  $\tilde{M}_{\text{sf,mp}} = 5$  produces the fastest resolution convergence, we used this as our “baseline” model and scanned for model variants around it in Section 5. Moreover, note that in this work, we are more interested in variations of the various quantities (BH luminosity functions, merger rates etc.) with respect to changing parameters, instead of the actual values for these quantities. These variations are not significantly affected by the decrease in convergence rate.

We now look at how the above trends impact the convergence of the observable statistics of black hole populations. Figures 21 and 22 show the mass functions (at  $z = 7$ ) and merger rates respectively. Let us start with  $M_{\text{seed}} = 1 \times 10^5 M_{\odot}/h$ . Here, we find that our predictions are indeed converging; i.e., differences between  $L_{\text{max}} = 11$  vs 12 predictions are smaller than that of  $L_{\text{max}} = 10$  vs 11; this is expected based on results from the previous paragraph. The mass functions converge to within factors of  $\sim 1.3$  and  $\sim 2$  for  $\tilde{M}_{\text{sf,mp}} = 5$  and 50 respectively by  $L_{\text{max}} = 11$ . The merger rates converge to within factors of  $\sim 2 - 4$  for





**Figure 20. Resolution convergence tests:** Distribution of seeding times for simulation boxes of different resolutions (different colors) at fixed set of seed parameters ( $M_{\text{seed}}$ ,  $\tilde{M}_{\text{sf,mp}}$ ,  $\tilde{M}_h$ ) for ZOOM\_REGION\_z5. Left and right panels correspond to  $\tilde{M}_{\text{sf,mp}} = 5$  and 50 respectively. Upper and lower panels show seed masses of  $1.25 \times 10^4 M_\odot/h$  and  $1.56 \times 10^3 M_\odot/h$  respectively.  $\tilde{M}_h = 3 \times 10^3$  in all the panels. The distributions approach convergence for  $L_{\text{max}} \geq 11$ . But note also that at  $z < 17$ , the rate of convergence is slightly lower for higher values of  $\tilde{M}_{\text{sf,mp}}$  and  $M_{\text{seed}}$ .

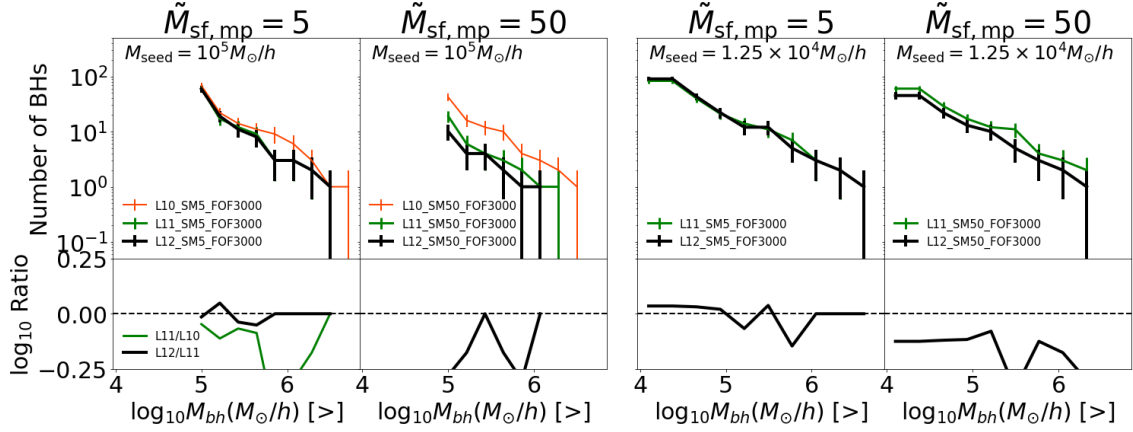


**Figure 21. Resolution convergence tests:** Cumulative mass functions at  $z = 7$  for simulation boxes of different resolutions (different colors) at fixed set of seed parameters ( $M_{\text{seed}}$ ,  $\tilde{M}_{\text{sf,mp}}$ ,  $\tilde{M}_h$ ) for ZOOM\_REGION\_z5.  $M_{\text{group}}^*$  and  $M_{\text{bh}}^{\text{group}}$  are stellar masses and black hole masses of halos.  $M_{\text{bh}}(>)$  is the minimum black hole mass above which the black hole counts are plotted in the right panels. The model parameters are the same as that of Figure 20 (see legends).  $M_* - M_{\text{bh}}$  relations and cumulative mass functions approach convergence with increasing resolution. The rate of convergence is slightly lower for higher values of  $\tilde{M}_{\text{sf,mp}}$  and  $M_{\text{seed}}$ .

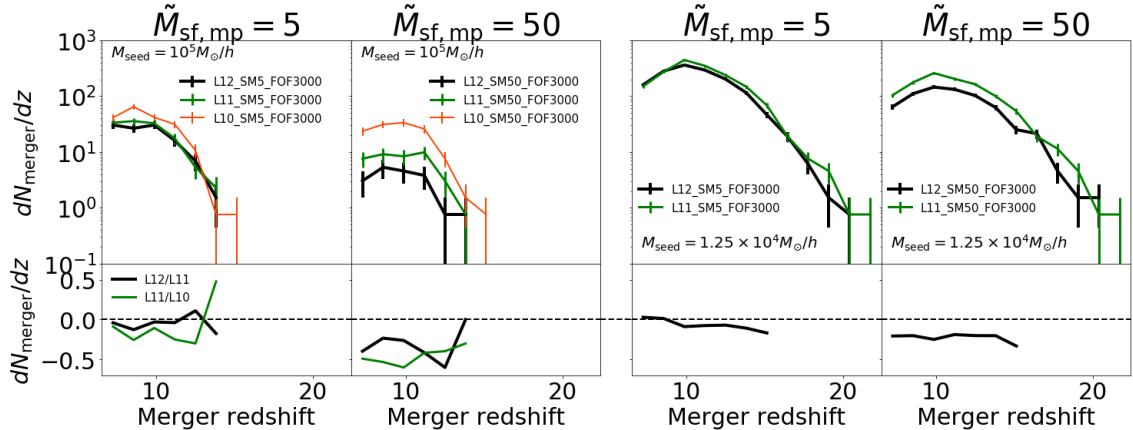


**Figure 22. Resolution convergence tests:** black hole merger rates for simulation boxes of different resolutions (different colors) at fixed set of seed parameters ( $M_{\text{seed}}$ ,  $\tilde{M}_{\text{sf,mp}}$ ,  $\tilde{M}_h$ ) for ZOOM\_REGION\_z5.  $L_{\text{bol}}(>)$  is the threshold bolometric luminosity. The model parameters are the same as that of Figure 20 (see legends). The merger rates approach convergence with increasing resolution. The rate of convergence is slightly lower for higher values of  $\tilde{M}_{\text{sf,mp}}$  and  $M_{\text{seed}}$ .

$\tilde{M}_{\text{sf,mp}} = 5$  and 50 by  $L_{\text{max}} = 11$  (albeit with very limited statistics for the latter). Resolution convergence is even better for  $M_{\text{seed}} = 1.25 \times 10^4 M_{\odot}/h$ ; this is consistent with expectations based on results from the previous paragraph and Figures 19 and 20.

Our analysis of resolution convergence reveals the following key findings:

- Our seed models produce black hole statistics (mass functions, luminosity functions and merger rates) that are reasonably well converged by  $L_{\text{max}} = 11$ ; this is largely driven by the resolution convergence of the star formation and metal enrichment.
- Our results converge more slowly with resolution for larger values of  $\tilde{M}_{\text{sf,mp}}$  or  $M_{\text{seed}}$ . This is due to a combination of two effects: 1) the resolution convergence of metal enrichment is slower than that of star formation, and 2) increasing  $\tilde{M}_{\text{sf,mp}}$  or  $M_{\text{seed}}$  pushes the seed formation to occur in regions with earlier metal enrichment.

## 7 SUMMARY AND CONCLUSIONS

In this work, we perform a systematic study to characterize the outcome of different black hole seed models using cosmological hydrodynamic zoom simulations. To this end, we built black hole models wherein the seed formation explicitly occurs in halos with star forming, metal poor gas and sufficiently deep potentials. All the other aspects of the galaxy formation model (which include star formation, feedback, metal enrichment) are identical to that of *IllustrisTNG*. Our main goal was to quantify the influence of various seed parameters on key SMBH observables such as the black hole masses, luminosities and merger rates. The key parameters of our seed models were namely:

- $M_{\text{seed}}$ : Black hole seed mass.
- $\tilde{M}_{\text{sf,mp}}$ : Minimum threshold of star forming, metal poor ( $Z < 10^{-4} Z_{\odot}$ ) gas mass (in units of  $M_{\text{seed}}$ ) in a halo. Only halos above this threshold are seeded with black holes.
- $\tilde{M}_h$ : Minimum threshold of total halo mass (in units of  $M_{\text{seed}}$ ). Only halos above this threshold are seeded with black holes.

We demonstrate that our model predictions approach resolution convergence in the zoom region; the convergence rate depends somewhat on the model parameters, as discussed in Section 6, but our results are reasonably converged for zoom resolutions of  $L_{\text{max}} \geq 11$ . Thus, we use this resolution for most of our analysis.

In our gas-based seed models, the onset of seed formation, driven by halo growth and the onset of star formation, occurs at redshifts ranging from  $\sim 12 - 25$  (depending on the model parameters). The rate of seed formation increases until its peak at  $z \sim 11$ , after which metal enrichment starts to suppress the seeding. Different seed parameters have a qualitatively distinct influence on seed formation. Owing to the scaling of the gas and halo mass thresholds with  $M_{\text{seed}}$  in our models, higher  $M_{\text{seed}}$  values cause the more massive seeds to form in halos with higher star forming, metal free mass and total halo mass. Increasing  $M_{\text{seed}}$  from  $1.56 \times 10^3 - 1 \times 10^6 M_{\odot}/h$  delays the onset of seeding and suppresses the number of seeds formed in each snapshot by up to factors of  $\sim 10$  and  $\sim 100$  for  $z \sim 7 - 11$  and  $z \gtrsim 11$ ,

respectively. Increasing  $\tilde{M}_{\text{sf,mp}}$  from 5 – 150 has very little effect on seed formation at  $z \gtrsim 15$ , but higher  $\tilde{M}_{\text{sf,mp}}$  values suppress seed formation by factors up to  $\sim 8$  at  $z \lesssim 15$ . Higher  $\tilde{M}_h$  causes seeds of a given mass to form in halos with higher total mass (or deeper potential wells); increasing  $\tilde{M}_h$  from  $10^3 - 10^4$  suppresses new seed formation at  $z \gtrsim 11 - 25$  by factors of  $\sim 10$ ; but no significant suppression is seen at  $z \sim 7 - 11$ . We now summarize the implications of our gas-based seed models on black hole growth, and their impact on the observable properties of the SMBH populations at  $z \geq 7$ .

- For all of our gas-based seed models, the majority of the black holes in our zoom region are primarily growing via black hole mergers. The contribution from gas accretion starts to become significant only at lower redshifts ( $z \lesssim 1$ ), particularly for  $\gtrsim 10^6 M_{\odot}/h$  black holes. That being said, the dominance of merger driven growth at  $z > 7$  may not persist around more extreme overdense regions; this will be investigated in future work.

- Lower seed masses produce dramatically higher black hole merger rates in our models at high redshift (by factors of  $\sim 10$  and  $\sim 10^3$  at  $z = 7$  and  $z = 15$ , respectively, as  $M_{\text{seed}}$  is decreased from  $10^5 M_{\odot}/h$  to  $1.56 \times 10^3 M_{\odot}/h$ ). This is driven in large part by the fact that the halo and gas mass thresholds are scaled to the seed mass in our models. When we consider only mergers between black holes above a fixed mass threshold that is  $\gtrsim 2$  times larger than the seed mass, the impact of the seed mass on the merger rate is much smaller (up to factors of  $\sim 2 - 3$ ). This is not surprising, given that the overall black hole counts above a fixed mass also vary by a similar amount.

- At fixed seed mass,  $\tilde{M}_{\text{sf,mp}}$  and  $\tilde{M}_h$  have distinct effects on the merger rates.  $\tilde{M}_h$  is the most important parameter at the highest redshifts ( $z \gtrsim 15$ ), where increasing  $\tilde{M}_h$  from  $10^3$  to  $10^4$  suppress the merger rates by factors of  $\gtrsim 100$ . At lower redshift, the star-forming, metal-poor gas mass criterion begins to have a larger influence seed formation. Specifically, an increase in  $\tilde{M}_{\text{sf,mp}}$  from 5-150 uniformly suppresses the overall merger rates by factors  $\sim 8$  over  $z \sim 7 - 15$  for  $M_{\text{seed}} = 1.25 \times 10^4 M_{\odot}/h$ . These findings suggest that the redshift distribution of black hole mergers probed by LISA may contain distinct signatures of the underlying seed formation channels.

- The black hole mass functions for different  $M_{\text{seed}}$  are similar for black hole masses  $\gtrsim 10^6 M_{\odot}/h$ . This is because lower mass seeds form earlier, which allows them enough time to grow and catch up with higher mass seeds that form later. When the seed mass is fixed, increasing  $\tilde{M}_{\text{sf,mp}}$  and  $\tilde{M}_h$  substantially suppresses the abundances of  $\gtrsim 10^6 M_{\odot}/h$ . For  $M_{\text{seed}} = 1.25 \times 10^4 M_{\odot}/h$ , the masses of the heaviest black holes are suppressed by factors of  $\sim 6$  when  $\tilde{M}_{\text{sf,mp}}$  is varied from 5 – 150; the suppression is by factors of  $\sim 10$  when  $\tilde{M}_h$  is varied from  $10^3 - 10^4$ . This is driven by the fact that black hole growth is completely dominated by mergers; in particular, fewer seeds are formed at higher values of  $\tilde{M}_{\text{sf,mp}}$  and  $\tilde{M}_h$  resulting in fewer mergers to facilitate black hole growth.

- AGN luminosity functions are less sensitive to variations in the seed model parameters; they are suppressed by up to factors  $\sim 2 - 3$  with respect to  $\tilde{M}_{\text{sf,mp}}$  (from 5-150) and  $\tilde{M}_h$  (from  $10^3 - 10^4$ ). An increase in  $M_{\text{seed}}$  from  $1.56 \times 10^3 - 10^5 M_{\odot}/h$  does not appreciably change our luminosity functions compared to our statistical uncertainties.

We conclude that the overall variation we see in the AGN luminosity functions amongst our seed models will be difficult to observe, even with sensitive future telescopes such as Lynx and JWST.

We must acknowledge that our analysis does not, by any means, encompass the complete parameter space of all possible seed models. Additionally, our limited volume does not allow us to probe the regime of the observed  $z > 6$  quasars as well as merger rates of massive ( $> 10^6 M_\odot/h$ ) black holes. Additionally, as with all zoom simulations, we are unable to provide volume independent statistics of the SMBH population (we shall address this using uniform volume simulations in our follow up paper). These factors overall make it difficult for us to directly comment on whether the seed models considered here would be distinguishable with EM or GW observables. Nevertheless, our results do clearly demonstrate that each of the seed model parameters considered here has a large impact on the black hole merger rate detectable with LISA. In contrast, the impact of varying seed parameters on the resulting AGN luminosity functions is relatively modest, indicating that it will likely be difficult to distinguish between these seeding models using high-redshift AGN surveys, even with future instruments such as Lynx.

Moreover, our results are going to be valuable for continued research because a similar exploration of the parameter space using uniform volume simulations (at volumes and resolutions similar to IllustrisTNG) will remain infeasible in the near future. To that end, when we do have predictions from a select few uniform volume simulations (with a specific choice of seed parameters), they can be combined with the results of this work to also make predictions for model variants (in a cost efficient manner).

Recall again that our numerical seed models are designed to be agnostic about which physical seed mechanism it is meant to represent. To that end, different values of the seed parameters can be representative of different physical seed formation scenarios. For example,  $1.56 \times 10^3 M_\odot/h$  seeds forming in  $\sim 10^6 - 10^7 M_\odot/h$  halos may better represent Pop III or NSC seeds (compared to DCBH seeds). On the other hand,  $1 \times 10^5 M_\odot/h$  seeds forming in  $\sim 10^8 - 10^9 M_\odot/h$  halos may better represent DCBHs. In future work, we plan to explore additional possible seeding criteria such as Lyman Werner intensity from nearby young stars, as well as the infall rates of gas towards halo centers. Finally, this work will drive continued development of gas-based seed models for large volume cosmological simulations. In particular, we plan to use these results for calibrating seed models for uniform volume (lower resolution) simulations. These results will also be useful for developing new SAMs. In particular, one can apply similar seed models to existing SAMs and compare the results to our work. In the process, one can test the various assumptions that are typically made in SAMs and may bring to light the ones that are most important in the context of black hole seed model development.

## APPENDIX A: SUPPRESSING SPURIOUS SEEDS

As mentioned in Section 2.1.1, black holes in our simulation are repositioned to the local potential minima within their

neighbor search radii. This may cause some halos to spuriously lose black holes during fly-by encounters around much larger halos, thereby causing these halos to spuriously seed a new BH. Here we describe the implementation for preventing spurious seeding in halos that have experienced a prior seeding event. At the time of new seed formation in a halo, the neighboring gas cells are “tagged”. More specifically, for every gas cell, we create a field called  $M_{\text{tag}}^{\text{gas}}$  and set it to be

$$M_{\text{tag}}^{\text{gas}} = M_{\text{seed}}/N_{\text{ngb}} \quad (\text{A1})$$

where  $N_{\text{ngb}}$  is the number of neighboring gas cells around the black hole seed.  $M_{\text{tag}}^{\text{gas}}$  is conserved during the refinement and derefinement of gas cells. It is also conserved when the gas cells are converted to star particles; i.e., for a newly formed star particle that was converted from a parent gas cell with  $M_{\text{tag}}^{\text{gas}}$ , we create a field called  $M_{\text{tag}}^{\text{star}}$  and assign

$$M_{\text{tag}}^{\text{star}} \equiv M_{\text{tag}}^{\text{gas}}. \quad (\text{A2})$$

Next, we compute the total amount of tagged gas and stars for every FOF group by defining  $M_{\text{tag}}^{\text{FOF}}$  as

$$M_{\text{tag}}^{\text{FOF}} \equiv \sum_{\text{gas}} M_{\text{tag}}^{\text{gas}} + \sum_{\text{stars}} M_{\text{tag}}^{\text{stars}} \quad (\text{A3})$$

where  $\sum_{\text{gas}}$  and  $\sum_{\text{stars}}$  represent a summation over all the gas cells and star particles respectively within the FOF group. Finally, for every FOF group we define a quantity  $f_{\text{tagged}}$  as

$$f_{\text{tagged}} \equiv M_{\text{tag}}^{\text{FOF}}/M_{\text{seed}}. \quad (\text{A4})$$

Now,  $f_{\text{tagged}}$  is constructed such that if a halo forms a black hole seed and does not lose or gain any tagged gas and stars during its subsequent evolution, then  $f_{\text{tagged}} = 1$ . However, a halo can potentially lose some of its tagged gas and stars due to the usual dynamical processes. Some of the gas can also be swallowed by the BH. Finally, a halo can also acquire tagged gas and stars from other halos. This overall implies that halos can have  $f_{\text{tagged}} < 1$  or  $f_{\text{tagged}} > 1$  depending on their assembly history. But the most important point is that the higher the value of  $f_{\text{tagged}}$ , the higher is the likelihood that the halo had undergone seed formation in the past. We therefore seek to suppress spurious seeding by setting a maximum value of  $f_{\text{tagged}}$ , above which the halos are prevented from seeding.

In Figures A1 and A2, we tested the impact of suppressing the spurious seeds with maximum  $f_{\text{tagged}}$  values of 0.1, 0.5, 0.9. Figure A1 shows the distribution of seeding redshifts. We find that our prescription reduces the number of seeding events (purple dashed lines vs. grey, cyan and green solid lines) by factors up to  $\sim 10$  for  $M_{\text{seed}} = 1.25 \times 10^4 M_\odot/h$ , particularly at  $z < 15$ . Figure A2 shows the merger rates, where we see that our prescription suppresses the number of mergers by factors  $\sim 10$  for  $M_{\text{seed}} = 1.25 \times 10^4 M_\odot/h$ . This implies that spurious seeding (if not suppressed) can substantially contaminate the SMBH populations. As we increase the seed masses (left vs right panels), spurious seeding is less prevalent. This is expected since higher mass seeds occur in more massive halos, which are less likely to lose their black holes during fly-by encounters.

Lastly, we also find that after the initial suppression (purple dashed lines vs. grey, cyan and green solid lines in Figures A1 and A2), further changes in the maximum  $f_{\text{tagged}}$  threshold from 0.1-0.9 (grey vs cyan vs green lines in A1 and A2) do not substantially impact the number of seeds and mergers. This

tells us that most halos that had past seeding events do not lose a substantial amount of their tagged gas and stars (and have  $f_{\text{tagged}} > 0.9$ ); this further certifies  $f_{\text{tagged}}$  as a very robust diagnostic parameter for identifying and suppressing spurious seeding events. For all the models presented in the remainder of the paper, we choose of maximum threshold of  $f_{\text{tagged}} < 0.5$  to allow the formation of black hole seeds.

## ACKNOWLEDGEMENTS

LB acknowledges support from National Science Foundation grant AST-1715413. LB and PT acknowledges support from NSF grant AST-1909933 and NASA ATP Grant 80NSSC20K0502. PT also acknowledges support from AST-200849. DN acknowledges funding from the Deutsche Forschungsgemeinschaft (DFG) through an Emmy Noether Research group (grant number NE 2441/1-1). MV acknowledges support through NASA ATP grants 16-ATP16-0167, 19-ATP19-0019, 19-ATP19-0020, 19-ATP19-0167, and NSF grants AST-1814053, AST-1814259, AST-1909831 and AST-2007355.

## DATA AVAILABILITY

The underlying data used in this work shall be made available upon reasonable request to the corresponding author.

## REFERENCES

- Amaro-Seoane P., et al., 2017, arXiv e-prints, [p. arXiv:1702.00786](#)  
 Anglés-Alcázar D., Davé R., Faucher-Giguère C.-A., Özel F., Hopkins P. F., 2017, *MNRAS*, **464**, 2840  
 Bañados E., et al., 2018, *Nature*, **553**, 473  
 Baker J., et al., 2019, arXiv e-prints, [p. arXiv:1907.06482](#)  
 Banik N., Tan J. C., Monaco P., 2019, *MNRAS*, **483**, 3592  
 Barausse E., 2012, *MNRAS*, **423**, 2533  
 Barnes J., Hut P., 1986, *Nature*, **324**, 446  
 Begelman M. C., Volonteri M., Rees M. J., 2006, *MNRAS*, **370**, 289  
 Bellovary J., Volonteri M., Governato F., Shen S., Quinn T., Wadsley J., 2011, *ApJ*, **742**, 13  
 Belotsky K. M., et al., 2019, *European Physical Journal C*, **79**, 246  
 Bernal J. L., Raccanelli A., Verde L., Silk J., 2018, *J. Cosmology Astropart. Phys.*, **2018**, 017  
 Blázquez-Calero G., et al., 2020, *MNRAS*, **491**, 1800  
 Bromm V., Loeb A., 2003, *ApJ*, **596**, 34  
 Buchner J., et al., 2015, *ApJ*, **802**, 89  
 Cautun M., et al., 2020, *MNRAS*, **494**, 4291  
 Chabrier G., 2003, *PASP*, **115**, 763  
 Chon S., Omukai K., 2020, *MNRAS*, **494**, 2851  
 Das A., Schleicher D. R. G., Basu S., Boekholt T. C. N., 2021a, *MNRAS*,  
 Das A., Schleicher D. R. G., Leigh N. W. C., Boekholt T. C. N., 2021b, *MNRAS*, **503**, 1051  
 Davé R., Anglés-Alcázar D., Narayanan D., Li Q., Rafieferantsoa M. H., Appleby S., 2019, *MNRAS*, **486**, 2827  
 Davies M. B., Miller M. C., Bellovary J. M., 2011, *ApJ*, **740**, L42  
 Davis B. L., Graham A. W., Seigar M. S., 2017, *MNRAS*, **471**, 2187  
 Dayal P., Rossi E. M., Shiralilou B., Piana O., Choudhury T. R., Volonteri M., 2019, *MNRAS*, **486**, 2336  
 DeGraf C., Sijacki D., 2020, *MNRAS*, **491**, 4973  
 Devecchi B., Volonteri M., Rossi E. M., Colpi M., Portegies Zwart S., 2012, *MNRAS*, **421**, 1465  
 Di Matteo T., Khandai N., DeGraf C., Feng Y., Croft R. A. C., Lopez J., Springel V., 2012, *ApJ*, **745**, L29  
 Ding X., Treu T., Silverman J. D., Bhowmick A. K., Menci N., Di Matteo T., 2020, *ApJ*, **896**, 159  
 Donnari M., et al., 2019, *MNRAS*, **485**, 4817  
 Dubois Y., Pichon C., Devriendt J., Silk J., Haehnelt M., Kimm T., Slyz A., 2013, *MNRAS*, **428**, 2885  
 Dubois Y., Peirani S., Pichon C., Devriendt J., Gavazzi R., Welker C., Volonteri M., 2016, *MNRAS*, **463**, 3948  
 Dunn G., Bellovary J., Holley-Bockelmann K., Christensen C., Quinn T., 2018, *ApJ*, **861**, 39  
 Fan X., et al., 2001, *AJ*, **122**, 2833  
 Feng Y., Di-Matteo T., Croft R. A., Bird S., Battaglia N., Wilkins S., 2016, *MNRAS*, **455**, 2778  
 Ferrarese L., Ford H., 2005, *Space Sci. Rev.*, **116**, 523  
 Ferrarese L., Merritt D., 2000, *ApJ*, **539**, L9  
 Fryer C. L., Woosley S. E., Heger A., 2001, *ApJ*, **550**, 372  
 Gardner J. P., et al., 2006, *Space Sci. Rev.*, **123**, 485  
 Gebhardt K., et al., 2000, *ApJ*, **539**, L13  
 Genel S., et al., 2014, *MNRAS*, **445**, 175  
 Genel S., et al., 2018, *MNRAS*, **474**, 3976  
 Grand R. J. J., et al., 2017, *MNRAS*, **467**, 179  
 Grand R. J. J., et al., 2020, *MNRAS*, **497**, 1603  
 Griffin A. J., Lacey C. G., Gonzalez-Perez V., Lagos C. d. P., Baugh C. M., Fanidakis N., 2020, *MNRAS*, **492**, 2535  
 Habouzit M., Volonteri M., Dubois Y., 2017, *MNRAS*, **468**, 3935  
 Habouzit M., et al., 2019, *MNRAS*, **484**, 4413  
 Habouzit M., Pisani A., Goulding A., Dubois Y., Somerville R. S., Greene J. E., 2020, *MNRAS*, **493**, 899  
 Habouzit M., et al., 2021, *MNRAS*, **503**, 1940  
 Hahn O., Abel T., 2011, *MNRAS*, **415**, 2101  
 Harms R. J., et al., 1994, *ApJ*, **435**, L35  
 Hirschmann M., Dolag K., Saro A., Bachmann L., Borgani S., Burkert A., 2014, *MNRAS*, **442**, 2304  
 Hopkins P. F., Quataert E., 2011, *MNRAS*, **415**, 1027  
 Hopkins P. F., Richards G. T., Hernquist L., 2007, *ApJ*, **654**, 731  
 Huang K.-W., Di Matteo T., Bhowmick A. K., Feng Y., Ma C.-P., 2018, *MNRAS*, **478**, 5063  
 Kaviraj S., et al., 2017, *MNRAS*, **467**, 4739  
 Kawasaki M., Kusenkov A., Yanagida T. T., 2012, *Physics Letters B*, **711**, 1  
 Khandai N., Di Matteo T., Croft R., Wilkins S., Feng Y., Tucker E., DeGraf C., Liu M.-S., 2015, *MNRAS*, **450**, 1349  
 Khlopov M. Y., Rubin S. G., Sakharov A. S., 2002, arXiv e-prints, [pp astro-ph/0202505](#)  
 Khlopov M. Y., Rubin S. G., Sakharov A. S., 2005, *Astroparticle Physics*, **23**, 265  
 Kormendy J., Ho L. C., 2013, *ARA&A*, **51**, 511  
 Kormendy J., Richstone D., 1992, *ApJ*, **393**, 559  
 Kroupa P., Subr L., Jerabkova T., Wang L., 2020, *MNRAS*, **498**, 5652  
 Kulkarni M., Visbal E., Bryan G. L., 2020, arXiv e-prints, [p. arXiv:2010.04169](#)  
 Lacy M., Ridgway S. E., Sajina A., Petric A. O., Gates E. L., Urrutia T., Storrie-Lombardi L. J., 2015, *ApJ*, **802**, 102  
 Latif M. A., Schleicher D. R. G., Hartwig T., 2016, *MNRAS*, **458**, 233  
 Lee J., et al., 2020, arXiv e-prints, [p. arXiv:2006.01039](#)  
 Libeskind N. I., et al., 2020, *MNRAS*, **498**, 2968  
 Lukić Z., Heitmann K., Habib S., Bashinsky S., Ricker P. M., 2007, *ApJ*, **671**, 1160  
 Luo Y., Ardaneh K., Shlosman I., Nagamine K., Wise J. H., Begelman M. C., 2018, *MNRAS*, **476**, 3523  
 Luo Y., Shlosman I., Nagamine K., Fang T., 2020, *MNRAS*, **492**, 4917



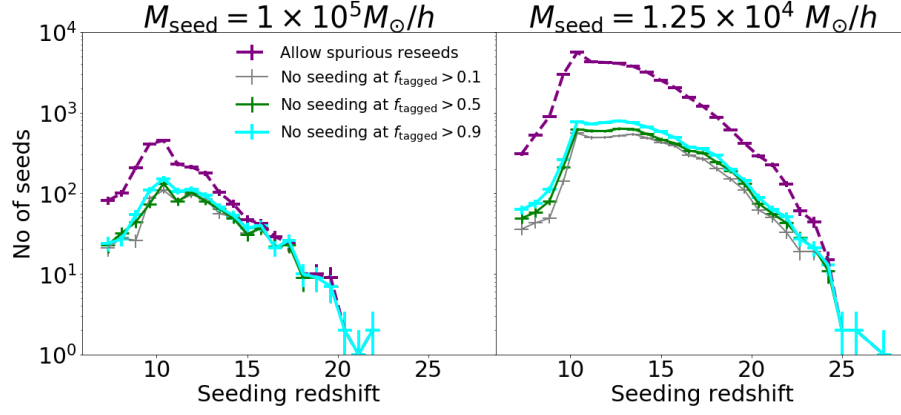


**Figure A1.** Distribution of seeding redshifts and how it is impacted by the various schemes detailed in Appendix A and Section 2.1.1. These runs were performed with  $\bar{M}_h = 10^3$ ,  $\bar{M}_{sf,mp} = 5$  (for ZOOM\_REGION\_z5). The solid lines correspond to cases where we have suppressed ‘seeding’ in halos that have a “memory” of a past seeding event.  $f_{\text{tagged}}$  for a halo (see Appendix A for details) is defined such that higher its value, higher is the likelihood that the halo hosted a black hole seed in the past. In particular, black hole seeding is suppressed in halos where  $f_{\text{tagged}}$  exceeds a maximum threshold. The cyan, green and grey lines correspond to runs where seeds were only allowed at  $f_{\text{tagged}} < 0.1, 0.5, 0.9$  respectively. Purple dashed line corresponds to a run where this “spurious seeding” is allowed. The difference between the purple dashed line and solid lines show that if we do not suppress the spurious seeds, it leads to substantially higher (by factors up to 10) number of seeding events. Additionally, we find that after the initial suppression compared to the purple dashed line, the distributions (cyan, purple and green lines) do not vary significantly with the specific maximum threshold chosen for  $f_{\text{tagged}}$  between 0.1 – 0.9. We therefore simply choose a fiducial maximum value of 0.5 for all our runs. Lastly, the prevalence of spurious seeds decreases with increasing  $M_{\text{seed}}$ .

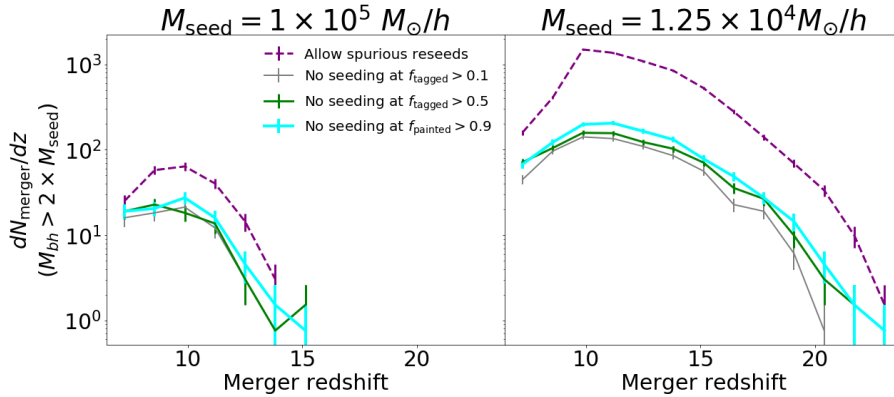


**Figure A2.** Distribution of merger rates and how it is impacted by the various schemes detailed in Appendix A and Section 2.1.1. These runs were performed with  $\bar{M}_h = 10^3$ ,  $\bar{M}_{sf,mp} = 5$  (for ZOOM\_REGION\_z5). Similar to Figure A1, solid lines correspond to cases where we have suppressed ‘seeding’ in halos that have a “memory” of a past seeding event. Cyan, green and grey lines correspond to  $f_{\text{tagged}} < 0.9, 0.5, 0.1$ . Purple dashed line corresponds to a run where this spurious seeding is allowed. Here also, we see that if the spurious seeds are not suppressed, the merger rates are overestimated by up to factors  $\sim 10$ . Additionally, we find that after the initial suppression compared to the purple dashed line, the merger rates (cyan, purple and green lines) do not vary significantly with the specific maximum threshold chosen for  $f_{\text{tagged}}$  between 0.1 – 0.9.

Lupi A., Colpi M., Devecchi B., Galanti G., Volonteri M., 2014, *MNRAS*, **442**, 3616  
Madau P., Rees M. J., 2001, *ApJ*, **551**, L27  
Magorrian J., et al., 1998, *AJ*, **115**, 2285  
Marconi A., Risaliti G., Gilli R., Hunt L. K., Maiolino R., Salvati M., 2004, *MNRAS*, **351**, 169  
Marinacci F., et al., 2018, *MNRAS*, **480**, 5113  
Marleau F. R., Clancy D., Habas R., Bianconi M., 2017, *A&A*, **602**, A28  
Marshall M. A., Ni Y., Di Matteo T., Wyithe J. S. B., Wilkins S., Croft R. A. C., Kuusisto J. K., 2020, *MNRAS*, **499**, 3819  
Merloni A., Heinz S., 2008, *MNRAS*, **388**, 1011  
Miyoshi M., Moran J., Herrnstein J., Greenhill L., Nakai N., Diamond P., Inoue M., 1995, *Nature*, **373**, 127

Mortlock D. J., et al., 2011, *Nature*, **474**, 616  
Mutlu-Pakdil B., Seigar M. S., Davis B. L., 2016, *The Astrophysical Journal*, **830**, 117  
Mutlu-Pakdil B., Seigar M. S., Hewitt I. B., Treuthardt P., Berrier J. C., Koval L. E., 2018, *MNRAS*, **474**, 2594  
Naiman J. P., et al., 2018, *MNRAS*, **477**, 1206  
Natarajan P., Pacucci F., Ferrara A., Agarwal B., Ricarte A., Zackrisson E., Cappelluti N., 2017, *ApJ*, **838**, 117  
Nelson D., et al., 2015, *Astronomy and Computing*, **13**, 12  
Nelson D., et al., 2018, *MNRAS*, **475**, 624  
Nelson D., et al., 2019a, *Computational Astrophysics and Cosmology*, **6**, 2  
Nelson D., et al., 2019b, *MNRAS*, **490**, 3234  
Ni Y., Di Matteo T., Feng Y., Croft R. A. C., Tenneti A., 2018,

- MNRAS*, **481**, 4877
- Pacucci F., Volonteri M., Ferrara A., 2015, *MNRAS*, **452**, 1922
- Pakmor R., Bauer A., Springel V., 2011, *MNRAS*, **418**, 1392
- Pakmor R., Pfrommer C., Simpson C. M., Kannan R., Springel V., 2016, *MNRAS*, **462**, 2603
- Pillepich A., et al., 2018a, *MNRAS*, **473**, 4077
- Pillepich A., et al., 2018b, *MNRAS*, **475**, 648
- Pillepich A., et al., 2019, *MNRAS*, **490**, 3196
- Planck Collaboration et al., 2016, *A&A*, **594**, A13
- Regan J. A., Johansson P. H., Wise J. H., 2014, *ApJ*, **795**, 137
- Regan J. A., Wise J. H., Woods T. E., Downes T. P., O’Shea B. W., Norman M. L., 2020, *The Open Journal of Astrophysics*, **3**, 15
- Reines A. E., Volonteri M., 2015, *ApJ*, **813**, 82
- Reines A. E., Greene J. E., Geha M., 2013, *ApJ*, **775**, 116
- Ricarte A., Natarajan P., 2018, *MNRAS*, **481**, 3278
- Rodriguez-Gomez V., et al., 2019, *MNRAS*, **483**, 4140
- Rubin S. G., Sakharov A. S., Khlopov M. Y., 2001, *Soviet Journal of Experimental and Theoretical Physics*, **92**, 921
- Sadowski A., Gaspari M., 2017, *MNRAS*, **468**, 1398
- Sales L. V., et al., 2015, *MNRAS*, **447**, L6
- Schaye J., et al., 2015, *MNRAS*, **446**, 521
- Schirra A. P., et al., 2020, arXiv e-prints, p. arXiv:2011.02501
- Schutte Z., Reines A. E., Greene J. E., 2019, *ApJ*, **887**, 245
- Sesana A., 2012, *Advances in Astronomy*, **2012**, 805402
- Sesana A., Volonteri M., Haardt F., 2007, *MNRAS*, **377**, 1711
- Shankar F., 2013, *Classical and Quantum Gravity*, **30**, 244001
- Shankar F., Salucci P., Granato G. L., De Zotti G., Danese L., 2004, *MNRAS*, **354**, 1020
- Shankar F., Weinberg D. H., Miralda-Escudé J., 2009, *ApJ*, **690**, 20
- Shen X., Hopkins P. F., Faucher-Giguère C.-A., Alexander D. M., Richards G. T., Ross N. P., Hickox R. C., 2020, *MNRAS*, **495**, 3252
- Sijacki D., Vogelsberger M., Genel S., Springel V., Torrey P., Snyder G. F., Nelson D., Hernquist L., 2015, *MNRAS*, **452**, 575
- Smith B. D., Regan J. A., Downes T. P., Norman M. L., O’Shea B. W., Wise J. H., 2018, *MNRAS*, **480**, 3762
- Spergel D., et al., 2015, arXiv e-prints, p. arXiv:1503.03757
- Springel V., 2010, *MNRAS*, **401**, 791
- Springel V., Hernquist L., 2003, *MNRAS*, **339**, 289
- Springel V., et al., 2018, *MNRAS*, **475**, 676
- Taylor P., Kobayashi C., 2015, *MNRAS*, **448**, 1835
- Tenneti A., Di Matteo T., Croft R., Garcia T., Feng Y., 2018, *MNRAS*, **474**, 597
- Tenneti A., Wilkins S. M., Di Matteo T., Croft R. A. C., Feng Y., 2019, *MNRAS*, **483**, 1388
- Terrazas B. A., Bell E. F., Henriques B. M. B., White S. D. M., Cattaneo A., Woo J., 2016, *ApJ*, **830**, L12
- The Lynx Team 2018, arXiv e-prints, p. arXiv:1809.09642
- Tinker J., Kravtsov A. V., Klypin A., Abazajian K., Warren M., Yepes G., Gottlöber S., Holz D. E., 2008, *ApJ*, **688**, 709
- Torrey P., et al., 2019, *MNRAS*, **484**, 5587
- Trebitsch M., et al., 2020, arXiv e-prints, p. arXiv:2002.04045
- Tremmel M., Governato F., Volonteri M., Quinn T. R., 2015, *MNRAS*, **451**, 1868
- Tremmel M., Karcher M., Governato F., Volonteri M., Quinn T. R., Pontzen A., Anderson L., Bellovary J., 2017, *MNRAS*, **470**, 1121
- Tundo E., Bernardi M., Hyde J. B., Sheth R. K., Pizzella A., 2007, *ApJ*, **663**, 53
- Übler H., et al., 2021, *MNRAS*, **500**, 4597
- Valiante R., Schneider R., Zappacosta L., Graziani L., Pezzulli E., Volonteri M., 2018, *MNRAS*, **476**, 407
- Vasudevan R. V., Fabian A. C., 2007, *MNRAS*, **381**, 1235
- Vogelsberger M., Genel S., Sijacki D., Torrey P., Springel V., Hernquist L., 2013, *MNRAS*, **436**, 3031
- Vogelsberger M., et al., 2014a, *MNRAS*, **444**, 1518
- Vogelsberger M., et al., 2014b, *Nature*, **509**, 177
- Vogelsberger M., Marinacci F., Torrey P., Puchwein E., 2020, *Nature Reviews Physics*, **2**, 42
- Volonteri M., 2012, *Science*, **337**, 544
- Volonteri M., Natarajan P., 2009, *Monthly Notices of the Royal Astronomical Society*, **400**, 1911–1918
- Volonteri M., Lodato G., Natarajan P., 2008, *MNRAS*, **383**, 1079
- Volonteri M., Dubois Y., Pichon C., Devriendt J., 2016, *MNRAS*, **460**, 2979
- Volonteri M., et al., 2020, *MNRAS*, **498**, 2219
- Wang F., et al., 2021, *ApJ*, **907**, L1
- Weinberger R., et al., 2017, *MNRAS*, **465**, 3291
- Weinberger R., et al., 2018, *MNRAS*, **479**, 4056
- Weinberger R., Springel V., Pakmor R., 2020, *ApJS*, **248**, 32
- Wise J. H., Regan J. A., O’Shea B. W., Norman M. L., Downes T. P., Xu H., 2019, *Nature*, **566**, 85
- Wu X.-B., et al., 2015, *Nature*, **518**, 512
- Xu H., Wise J. H., Norman M. L., 2013, *ApJ*, **773**, 83
- Yoshida N., Abel T., Hernquist L., Sugiyama N., 2003, *ApJ*, **592**, 645
- Zhu Q., Li Y., Li Y., Maji M., Yajima H., Schneider R., Hernquist L., 2020, arXiv e-prints, p. arXiv:2012.01458